The Astrophysical Journal, 962:72 (15pp), 2024 February 10 https://doi.org/10.3847/1538-4357/ad1182

A Survey of Lyα Emission around Damped Lyα Absorbers at $z \approx 2$ with the Keck Cosmic Web Imager

Grecco A. Oyarzún[1,8], Marc Rafelski[1,2], Nissim Kanekar[3], J. Xavier Prochaska[4,5], Marcel Neeleman[6], and Regina A. Jorgenson[7]
[1] The William H. Miller III Department of Physics & Astronomy, Johns Hopkins University, Baltimore, MD 21218, USA; goyarzu1@jhu.edu
[2] Space Telescope Science Institute, 3700 San Martin Drive, Baltimore, MD 21218, USA
[3] National Centre for Radio Astrophysics, Tata Institute of Fundamental Research, Pune University, Pune 411007, India
[4] Department of Astronomy & Astrophysics, UCO/Lick Observatory, University of California, 1156 High Street, Santa Cruz, CA 95064, USA
[5] Kavli Institute for the Physics and Mathematics of the Universe (Kavli IPMU), 5-1-5 Kashiwanoha, Kashiwa, 277-8583, Japan
[6] National Radio Astronomy Observatory, 520 Edgemont Road, Charlottesville, VA 22903, USA
[7] Maria Mitchell Observatory, Nantucket, MA, USA
Received 2023 November 2; revised 2023 November 27; accepted 2023 November 29; published 2024 February 8

Abstract

We present Keck Cosmic Web Imager Lyα integral field spectroscopy of the fields surrounding 14 damped Lyα absorbers (DLAs) at $z \approx 2$. Of these 14 DLAs, nine have high metallicities ([M/H] > -0.3), and four of those nine feature a CO-emitting galaxy at an impact parameter $\lesssim$30 kpc. Our search reaches median Lyα line flux sensitivities of $\sim 2 \times 10^{-17}$ erg s^{-1} cm^{-2} over apertures of $\sim$6 kpc and out to impact parameters of $\sim$50 kpc. We recover the Lyα flux of three known Lyα-emitting H I-selected galaxies in our sample. In addition, we find two Lyα emitters at impact parameters of $\approx$50–70 kpc from the high-metallicity DLA at $z \approx 1.96$ toward QSO B0551-366. This field also contains a massive CO-emitting galaxy at an impact parameter of $\approx$15 kpc. Apart from the field with QSO B0551-366, we do not detect significant Lyα emission in any of the remaining eight high-metallicity DLA fields. Considering the depth of our observations and our ability to recover previously known Lyα emitters, we conclude that H I-selected galaxies associated with high-metallicity DLAs at $z \approx 2$ are dusty and therefore might feature low Lyα escape fractions. Our results indicate that complementary approaches—using Lyα, CO, Hα, and [C II] 158 μm emission—are necessary to identify the wide range of galaxy types associated with $z \approx 2$ DLAs.

Unified Astronomy Thesaurus concepts: Galaxy evolution (594); Galaxy formation (595); Damped Lyα systems (349); Lyα galaxies (978); Galaxies (573); Quasars (1319); Circumgalactic medium (1879); Intergalactic clouds (809); Neutral hydrogen clouds (1099); Intergalactic gas (812); Intergalactic medium (813); Quasar-galaxy pairs (1316)

1. Introduction

The H I cycle within and around galaxies is a critical component in our models of galaxy formation and evolution. We know that galaxies must acquire H I from the intergalactic medium in order to sustain their star formation (Kereš et al. 2005; Prochaska et al. 2005; Walter et al. 2020). The inflow of H I is counteracted by outflows of metal-enriched gas powered by active galactic nuclei and/or the late stages of stellar evolution, thereby regulating the rate at which galaxies form their stars (e.g., Kereš et al. 2005; Tumlinson et al. 2017). Furthermore, the removal of H I from galaxies through environment-driven processes (Gunn & Gott 1972; Kawata & Mulchaey 2008; Cortese et al. 2021) is often invoked to explain the quenched fractions and assembly histories of satellite galaxies (e.g., Pasquali et al. 2010; Wetzel et al. 2013; Gallazzi et al. 2021; Trussler et al. 2021; Werle et al. 2022; Oyarzún et al. 2023).

To characterize the H I content in and around galaxies at low redshift, we often turn to studies of 21 cm emission (e.g., Verheijen 2001; Begum et al. 2008; Walter et al. 2008; Chung et al. 2009; Heald et al. 2011; Catinella et al. 2018). Single-dish 21 cm studies have yielded H I emission-line detections for thousands of galaxies at low redshifts (e.g., Zwaan et al. 2005; Haynes et al. 2018), while 21 cm mapping studies have been used to, for example, quantify the star formation efficiency in nearby galaxies (Leroy et al. 2008), measure the sizes of H I disks (e.g., Wang et al. 2016), determine galaxy rotation curves (e.g., Begum et al. 2008; Walter et al. 2008), and search for extraplanar gas (e.g., Heald et al. 2011). However, the faintness of the 21 cm transition has so far prevented us from detecting H I in emission from individual galaxies beyond $z \approx 0.4$ (Fernández et al. 2016) or in stacked imaging beyond $z \approx 1.4$ (Chowdhury et al. 2020, 2021, 2022a).

Alternatively, absorption signatures in the spectra of background quasars (QSOs) produced by high H I column density gas (damped Lyα absorbers, or DLAs; Wolfe et al. 2005) remain the quintessential technique for studying H I at high redshift. Through DLA characterization, we have been able to constrain the column densities, metallicities, kinematics, dust depletion, molecular fractions, and gas temperatures of H I reservoirs up to $z \sim 5.5$ (e.g., Prochaska & Wolfe 1997; Noterdaeme et al. 2008; Neeleman et al. 2013; Kanekar et al. 2014; Neeleman et al. 2015; Balashev et al. 2017; Klimenko et al. 2020). Moreover, DLAs have been instrumental in determining the evolution of the metal enrichment and cosmic H I mass density since $z \approx 5$ (e.g., Noterdaeme et al. 2012; Rafelski et al. 2012; Jorgenson

[8] Corresponding author.

et al. 2013; Prochaska et al. 2013; Rafelski et al. 2014; Crighton et al. 2015; Rao et al. 2017), connecting with estimates at lower redshifts from 21 cm observations (e.g., Jones et al. 2018; Bera et al. 2019).

On the other hand, it has been challenging to associate the properties of H I measured in absorption with the properties of galaxies measured in emission. DLA galaxies are typically much fainter than the background QSOs, and they are found over a wide range of impact parameter (b), which makes the identification of the galaxy through standard optical imaging and spectroscopy very challenging. Despite many searches, only about a dozen galaxies associated with DLAs at $z \gtrsim 2$ were detected in over a quarter of a century (e.g., Møller & Warren 1993; Fumagalli et al. 2015). Fortunately, the detection rate has since increased. After it was realized that the stellar mass and gas-phase metallicity relation (e.g., Tremonti et al. 2004) also holds for absorption-selected systems (e.g., Møller et al. 2004; Ledoux et al. 2006; Fynbo et al. 2008), studies in the rest-frame UV/optical have started to target high-metallicity DLAs ($[\mathrm{M/H}] \gtrsim -1.3$) with great success (e.g., Krogager et al. 2017).

At the same time, the advent of the Atacama Large Millimeter/submillimeter Array (ALMA) has enabled a search for DLA galaxies at millimeter and submillimeter wavelengths, where the QSOs are much fainter and line emission from cool or cold gas can be luminous. ALMA and Northern Extended Millimetre Array (NOEMA) images have been used to identify a further dozen star-forming counterparts of high-metallicity ($[\mathrm{M/H}] > -1.3$) DLAs through their CO emission at $z \approx 2$ or their [C II] 158 μm emission at $z \approx 4$ (Neeleman et al. 2017; Fynbo et al. 2018; Neeleman et al. 2018, 2019; Kanekar et al. 2020; Kaur et al. 2022b).

Although searches for DLA galaxies in the CO and [C II] 158 μm transitions have been shown to be quite efficient, the downside is that they are bound to miss galaxies with high CO-to-H_2 conversion factors or with relatively low molecular gas masses ($\lesssim$1–5 $\times$ 10^{10} $M_\odot$; Neeleman et al. 2019; Kanekar et al. 2020; Kaur et al. 2022b). Such undetected galaxies could reside at lower impact parameters than mm-detected galaxies, perhaps explaining why the impact parameters between mm-detected galaxies and DLA sightlines—$b < 30$ kpc at $z \approx 2$ and $b \gtrsim 25$ kpc at $z \approx 4$ (Neeleman et al. 2017, 2018, 2019; Kanekar et al. 2020)—can exceed the sizes of H I gas reservoirs at $z \approx$ 2–4 in simulations (<30 kpc; Rhodin et al. 2019; Stern et al. 2021).

To search for galaxies with high CO-to-H_2 conversion factors and/or low molecular gas masses, we can turn to rest-frame UV/optical emission. Among the standout emission lines at these wavelengths is Lyα, which is produced in H II regions by recombining H I gas. However, only ≈20%–25% of Lyman-break galaxies (LBGs; Steidel et al. 1996, 1999; Shapley et al. 2003; Steidel et al. 2003; Stark et al. 2009) at $z \approx 2$ show Lyα emission (e.g., Cassata et al. 2015). This is presumably due to the ease with which Lyα is scattered by H I and absorbed by dust grains (e.g., Dijkstra & Kramer 2012; Duval et al. 2014; Rivera-Thorsen et al. 2015; Gronke & Dijkstra 2016; Gronke et al. 2016). As a result, the equivalent width of the Lyα line is particularly high in galaxies with low H I gas covering fractions and low dust extinctions, i.e., low-stellar-mass ($M_* \lesssim 10^{10}$ $M_\odot$) galaxies (e.g., Oyarzún et al. 2016, 2017).

For these reasons, Lyα searches have been exploited to detect DLA galaxies down to much lower metallicities ($[\mathrm{M/H}] \lesssim -1.3$) than mm-wave transitions (e.g., Møller et al. 2004; Mackenzie et al. 2019; Lofthouse et al. 2023). To search for Lyα emission at the DLA redshift, early searches used narrowband imaging, yielding a few tentative detections (e.g., Smith et al. 1989; Lowenthal et al. 1991; Giavalisco et al. 1994; Fynbo et al. 2003; Kulkarni et al. 2006; Grove et al. 2009; Fynbo et al. 2023). More recently, Lyα searches have capitalized on the sensitivities of new state-of-the-art optical integral field units (IFUs; e.g., Christensen et al. 2007; Péroux et al. 2011, 2012; Fumagalli et al. 2017; Mackenzie et al. 2019; Lofthouse et al. 2023). For instance, Fumagalli et al. (2017) used the Multi Unit Spectroscopic Explorer (MUSE) on the Very Large Telescope (VLT) to identify three Lyα emitting sources associated with a DLA at $z \sim 3.25$. Building on this result, subsequent surveys with VLT/MUSE have found more than 20 Lyα emitters out to impact parameters of ≈300 kpc in the fields of ≈15 low-metallicity DLAs at $z \approx 3$ (e.g., Mackenzie et al. 2019; Lofthouse et al. 2020, 2023).

Motivated by the success of recent searches in Lyα with IFUs, in this work we searched for Lyα emission in the fields of 14 DLAs—nine of which have been previously studied in mm-wave CO emission—with the Keck Cosmic Web Imager Integral Field Spectrograph (KCWI; Morrissey et al. 2018) on the Keck II telescope. KCWI is an outstanding instrument for this search because of its high sensitivity at the observed-frame wavelength of $z \approx 2$ Lyα emission ($\lambda \approx 4500$ Å). Moreover, the effective field of view of ∼100 kpc enables us to cover the impact parameter range expected for the primary emission counterparts of high H I column density absorbers ($\lesssim$30 kpc; e.g., Rahmati & Schaye 2014; Rhodin et al. 2019).

The paper is structured as follows. We define our target sample of DLAs and describe the observations in Sections 2 and 3. We detail our methodology to identify and characterize Lyα emission in Section 4. We present our results in Section 5, discuss their interpretation in Section 6, and provide a summary of the paper in Section 7. Throughout the paper, we assume $H_0 = 70\ \mathrm{km\ s^{-1}\ Mpc^{-1}}$. All magnitudes are reported in the AB system (Oke & Gunn 1983).

2. The Sample

Rafelski et al. (2012, 2014) employed the Echellette Spectrograph and Imager (ESI; Sheinis et al. 2002) and the High Resolution Echelle Spectrometer (HIRES; Vogt et al. 1994) on the Keck Telescopes to obtain high-resolution spectroscopy for 50 QSOs. Novel in their analysis was the DLA selection being based solely on H I column density ($N_{\mathrm{H\,I}}$), thus avoiding any metallicity biases. As part of their work, they also reanalyzed a collection of QSO spectra from the literature selected not to have a metallicity bias. It is from this sample that the majority of the DLAs in our work originate (B0458-020, J2206-1958a,B1228-113, B0201+365, B0551-366, B1230-101, J0453-1305, and J2206-1958b). In addition, three high-metallicity DLAs in our sample—J1305+0924, Q1755+578, and J1013+5615—were characterized by Berg et al. (2015). Completing our sample are J2222-0946, J2225+0527, and J1709+3258, which were characterized by Fynbo et al. (2010), Krogager et al. (2016), and Kaplan et al. (2010), respectively. The properties of our DLAs—i.e., redshifts, $N_{\mathrm{H\,I}}$, and metallicities— are presented in Table 1 and in Figure 1. As is clear from the figures, our 14 target DLAs are dominated by high-metallicity absorbers ($[\mathrm{M/H}] > -0.3$).

Table 1
Sample

QSO	R.A.	Decl.	m_{qso}	z_{qso}	Subsample	Exp. Time (hr)
B0458-020	05:01:12.80	−01:59:14.25	18.69	2.29	control	1
J2206-1958a[a]	22:08:52.07	−19:43:59.86	16.82	2.57	control/CO	1.5
J2222-0946	22:22:56.11	−09:46:36.28	18.04	2.93	control/CO	1
J1305+0924	13:05:42.77	09:24:27.75	18.95	2.04	CO	1
B1228-113	12:30:55.56	−11:39:09.79	19.63	3.53	CO	1
B0201+365	02:04:55.60	36:49:17.99	18.04	2.91	CO	1
B0551-366	05:52:46.18	−36:37:27.60	16.98	2.32	CO	0.83
J2225+0527	22:25:14.70	05:27:09.06	17.84	2.32	CO	1
J1709+3258	17:09:09.28	32:58:03.40	19.17	1.89	CO	0.5
B1230-101	12:33:13.16	−10:25:18.44	19.26	2.39	CO	0.83
J0453-1305	04:53:13.57	−13:05:55.09	16.99	2.26	blind	0.66
J2206-1958b[a]	22:08:52.07	−19:43:59.86	16.82	2.57	blind	1.5
Q1755+578	17:56:03.63	57:48:47.99	18.55	2.11	blind	1.17
J1013+5615	10:13:36.38	56:15:36.41	18.61	3.63	blind	1

Notes. The columns correspond to the QSO sightline identifier (1), QSO R.A. (2), QSO decl. (3), magnitude of the QSO in the g-band measured by the Gaia Collaboration et al. (2023) (4), redshift of the QSO (5), DLA subsample (6), and exposure time (7).
[a] There are two DLAs along the sightline of J2206-1958.

2.1. The CO Subsample

By design, our sample of target DLAs is dominated by systems with ancillary CO observations. These observational campaigns were conducted with ALMA (Kanekar et al. 2020), NOEMA (Kaur et al. 2022b), and the Karl G. Jansky Very Large Array (JVLA; B. Kaur et al. 2023, in preparation). Those authors searched for mm-wave redshifted CO(1−0), CO(2−1), CO(3−2), or CO(4−3) emission from the fields of 20 high-metallicity ($[M/H] \gtrsim -1.0$) DLAs at $z \approx 1.7$–2.6. They identified six robust ($>5\sigma$ significance) and two tentative (4σ–5σ) detections of redshifted CO emission, obtaining a ≈50% CO detection rate of galaxies around their highest-metallicity DLAs ($[M/H] \gtrsim -0.35$). Five of the CO detections have impact parameters in the range $b = 5$–30 kpc (Neeleman et al. 2018; Kanekar et al. 2020; Kaur et al. 2022b). The sixth CO detection is at $b \approx 100$ kpc (Fynbo et al. 2018; Kanekar et al. 2020) in a system at $z \approx 2.58$ where a DLA galaxy has been identified at $b \approx 16$ kpc (Q0918+1636; Fynbo et al. 2011, 2013). For the 13 CO nondetections, the median 3σ upper limit on the molecular gas mass is $\approx 1.2 \times 10^{10}\ M_{\odot}$, for a CO-to-$H_2$ conversion factor of $\alpha_{CO} = 4.36\ M_{\odot}\ (\mathrm{K\ km\ s^{-1}\ pc^2})^{-1}$ (e.g., Bolatto et al. 2013). Of the 14 DLAs in our sample, nine have CO studies, with four CO detections, two tentative detections, and three nondetections see (Tables 1 and 2). We will refer to these nine DLAs as the CO subsample throughout.

2.2. The Control Subsample

Earlier Lyα searches for galaxies at low impact parameters have obtained detections in two of the DLAs in the CO subsample. Lyα emission in the field of the $z = 2.3543$ DLA toward J2222-0946 was first reported, at $b \approx 6$ kpc, by Fynbo et al. (2010; see also Krogager et al. 2013, 2017). The $z = 1.9200$ DLA toward J2206-1958 also has an associated Lyα-emitting galaxy (at $b \lesssim 6$ kpc; Møller et al. 2002). No CO emission was detected in either of these fields by Kanekar et al. (2020). A third DLA in our sample, this time without ancillary CO observations, has also been detected in Lyα. This galaxy is at $z = 2.0395$ toward B0458-020 and at an impact parameter of $b \lesssim 3$ kpc (Møller et al. 2004; Krogager et al. 2017). Together, the three known Lyα emitters in the fields of J2222-0946, J2206-1958, and B0458-020 constitute our control sample. They were used to assess the efficacy of our survey and to search for additional Lyα associations at larger impact parameters.

2.3. The "Blind" Subsample

The remaining four DLA fields (Table 1) compose the "blind" sample, i.e., absorbers without earlier searches for the associated galaxies. One of these four DLAs lies toward J2206-1958, a sightline containing one of our control DLAs. The remaining three blind-sample DLAs were observed due to their convenient celestial coordinates in the context of our observational strategy. They will be the targets of future CO observations with ALMA, NOEMA, and/or the JVLA.

3. Observations

The 14 DLA fields in this work were observed with the Keck Cosmic Web Imager Integral Field Spectrograph (KCWI; Morrissey et al. 2018), on the Keck II telescope. KCWI is optimized for observations in the 3500–5600 Å spectral range with resolution $R = 1000$–20,000. The size of a spaxel is ∼0.″7, which corresponds to a physical size of ∼6 kpc at $z \sim 2$. We opted for the configuration with a 20″ × 16″ field of view at a spatial resolution of 0.″7 and with a spectral resolution of R∼2000 or R∼4000, depending on the target. At $z \sim 2$, this configuration corresponds to a field of view of ∼170 kpc × 130 kpc and a spatial resolution of ∼6 kpc.

The first set of KCWI observations was conducted in 2019 September and October, with later observing runs in 2021 February and April. The on-target exposure time varied between 0.5 and 1.5 hr, with DLAs with ancillary CO observations given priority. We obtained line flux sensitivities of ≈ 0.1–$5 \times 10^{-16}\ \mathrm{erg\ s^{-1}\ cm^{-2}}$ at S/N = 5, depending on the exposure time and the DLA redshift (i.e., the redshifted Lyα wavelength).

The KCWI data were analyzed with PypeIt,[9] a Python package designed for the semi-automated reduction of astronomical spectroscopic data.[10] We used the built-in routines to perform bias subtraction, dark correction, and trace

[9] https://pypeit.readthedocs.io/en/release/
[10] https://pypeit.readthedocs.io/en/release/spectrographs/keck_kcwi.html

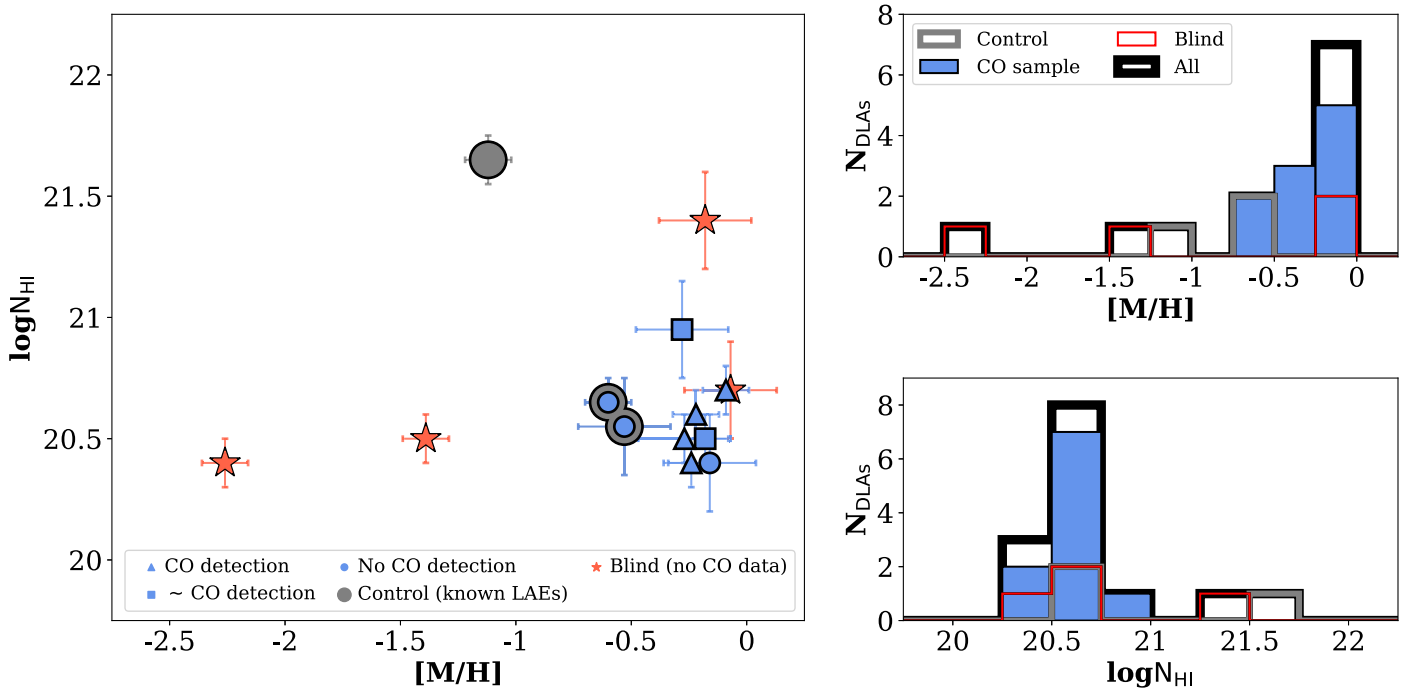

Figure 1. The sample. Left: Distribution of the DLAs in metallicity–$N_{\rm H\,I}$ space. Control DLA galaxies (i.e., known Lyα emitters) are plotted as large gray circles. DLAs previously targeted for CO observations are denoted with the small blue markers. Nondetections in CO are plotted as circles, potential CO detections as squares, and CO detections as triangles. DLAs without mm observations are plotted as red stars. Right: Histograms of the metallicities and H I column densities of our 14 DLAs. The full sample is plotted in black, control DLA galaxies in gray, DLAs with CO observations in blue, and DLAs without known prior Lyα or CO observations in red.

pattern identification. For wavelength calibration, we used FeAr lamps. The flat-fielding of the data accounted for pixel-by-pixel variations and the dome illumination pattern. The faintness of our targets allowed PypeIt to use the science frames themselves to perform sky subtraction. Bright objects, such as the QSO in each field, were detected and masked in the computation of the sky model. The astrometric solution of the data cubes was revised using the coordinates of the QSOs.

3.1. Flux Calibration

Observations of standard stars ($m \sim 10$) prior to or after the science exposures were used for flux calibration. We used PypeIt to compute the flux sensitivity curves from these standard stars. The first step of the process was to flux calibrate the data cubes of the standard stars. We verified that this step was performed appropriately by comparing the flux-calibrated standard data cubes with the well-characterized standard spectra. Then, the flux-calibrated standard star data cubes were used as the input sensitivity curves in the coaddition of all the data cubes (i.e., exposures) for each target.

To quantify the accuracy of our flux calibration, we searched for publicly available observations of the QSOs ($m \sim 18$; Table 1) in our sample. Four of the QSOs—J2222-0946, J1305+0924, J1709+3258, and J1013+5615—were observed in the Baryon Oscillation Spectroscopic Survey (BOSS) of the Sloan Digital Sky Survey (SDSS; Alam et al. 2015). We found that our flux calibration is consistent with that of SDSS/BOSS within a factor of ~2. To maximize the accuracy of our flux calibration, we estimated a flux-correction factor by maximizing the likelihood between the KCWI and the SDSS/BOSS spectra. An optimal flux-correction factor of 1.8 was found and used to rescale our flux-calibrated spectra. The dispersion among these measurements indicates that our flux calibration has a standard error of 12%. All errors on the line fluxes reported in this paper include this factor of 0.12. Finally, all fluxes were corrected for Milky Way extinction using the Fitzpatrick (1999) extinction curve, the dust reddening maps from Schlegel et al. (1998), and the reddening-to-A_V conversion tabulated in Schlafly & Finkbeiner (2011).

4. Methodology

4.1. Subtraction of the Sky Background and the QSO Continuum

Figure 2 shows the fully reduced KCWI spectra toward each target QSO centered at, and zoomed in on, the redshifted Lyα absorption line of each of the 14 DLAs. Before searching for emission lines at the DLA redshift, characterization of the QSO emission was required. We started by constructing a QSO continuum model for the data cube of every target. To do this, we computed $\phi_{\rm qso}(\lambda)$, a least-squares Chebyshev series fit to the QSO continuum in the brightest spaxel. Then, $\phi_{\rm qso}(\lambda)$ was scaled throughout the data cube to produce the initial continuum model cube,

$$\mathcal{C}_{\rm qso}(x, y, \lambda) = A(x, y)\phi_{\rm qso}(\lambda), \quad (1)$$

where $A(x, y)$ is the spaxel-dependent QSO continuum scaling factor. The spaxel-dependent error in the spectra—$\sigma(x, y, \lambda)$—was then used to estimate

$$\mathcal{SN}_{\rm qso}(x, y) = \frac{1}{n}\sum_{\lambda}^{n} \frac{\mathcal{C}_{\rm qso}(x, y, \lambda)}{\sigma(x, y, \lambda)}, \quad (2)$$

i.e., the mean signal-to-noise ratio (S/N) of the QSO continuum throughout the data cube. Thresholds in $\mathcal{SN}_{\rm qso}(x, y)$ were imposed to identify spaxels affected by the

Table 2
Survey Results

QSO	Sample	z_{abs}	$\log N_{HI}$ ($\log cm^{-2}$)	[M/H]	z_{em}	$F_{Ly\alpha}$ (10^{-17} erg s^{-1} cm^{-2})	$L_{Ly\alpha}$ (10^{42} erg s^{-1})	b (kpc)
B0458-020	control	2.0396	21.65 ± 0.1	-1.12 ± 0.1	2.041	6.4 ± 3 (6.3σ)	2 ± 1	0 ± 6
J2206-1958a†	control/CO(×)	1.9200	20.65 ± 0.1	-0.60 ± 0.1	1.923	14 ± 6 (6.5σ)	4 ± 1.7	12 ± 6
J2222-0946	control/CO(×)	2.3543	20.55 ± 0.2	-0.53 ± 0.2	2.357	13 ± 5 (19.3σ)	6 ± 2	8 ± 4
J1305+0924	CO(×)	2.0184	20.4 ± 0.2	-0.16 ± 0.2	⋯	<2.2	<0.7	⋯
B1228-113	CO(✓)	2.1928	20.6 ± 0.1	-0.22 ± 0.1	⋯	<3.7	<1.4	⋯
B0201+365	CO(✓)	2.4628	20.4 ± 0.1	-0.24 ± 0.1	⋯	<1.5	<0.8	⋯
B0551-366	CO(✓)	1.9622	20.5 ± 0.1	-0.27 ± 0.2	1.963	12 ± 5 (9.2σ)	3.4 ± 1.4	53 ± 4
					1.957	17 ± 6 (6.4σ)	5 ± 1.8	70 ± 4
J2225+0527	CO(✓)	2.1310	20.7 ± 0.1	-0.09 ± 0.1	⋯	<2.5	<0.9	⋯
J1709+3258	CO(∼)	1.8300	20.95 ± 0.2	-0.28 ± 0.2	⋯	<60	<15	⋯
B1230-101	CO(∼)	1.9314	20.5 ± 0.1	-0.18 ± 0.1	⋯	<14	<3.9	⋯
J0453-1305*	blind	2.0666	20.5 ± 0.1	-1.39 ± 0.1	2.067*	4.2 ± 3* (4σ)	1.4 ± 1*	6 ± 6*
J2206-1958b†	blind	2.0762	20.4 ± 0.1	-2.26 ± 0.1	⋯	<2	<0.7	⋯
Q1755+578	blind	1.9692	21.4 ± 0.2	-0.18 ± 0.2	⋯	<4.8	<1.4	⋯
J1013+5615	blind	2.2831	20.7 ± 0.2	-0.07 ± 0.2	⋯	<1.3	<0.6	⋯

Notes. The columns correspond to the QSO sightline identifier (1), DLA subsample (2), redshift of the DLA (3), H I column density of the DLA (4), metallicity of the DLA (5), redshift of the emission (Lyα; 6), Lyα line flux (S/N > 5; 7), Lyα luminosity (8), and impact parameter of the galaxy (Lyα; 9). The symbols in the second column denote significant detections (✓), tentative detections (∼), and nondetections (×) in the CO imaging. There are two DLAs along the sightline of J2206-1958 (†). The DLA along B0551-366 has two detections in Lyα. The DLA along J0453-1305 is a tentative Lyα detection (*). The uncertainty on the Lyα line flux includes the error on the absolute flux calibration, and thus it should not be used to estimate the significance of the line. The signal-to-noise ratios of the individual detections are listed in parenthesis, next to the Lyα flux measurements.

QSO continuum. Depending on the target, we found the optimal value for the threshold—determined through visual inspection—to vary between 5 and 14.

In order to estimate the background emission throughout each cube, all spaxels affected by QSO emission were masked. After masking, the median spectrum across each data cube was fitted with a Chebyshev series to obtain the background model $\mathcal{C}_{sky}(\lambda)$. Implementation of the median instead of the mean ensured that no serendipitous background sources affected our estimate of $\mathcal{C}_{sky}(\lambda)$. For each field, a background-subtracted data cube was then computed, which then was used to measure $\mathcal{C}_{qso}(x, y, \lambda)$ again; this time without contributions from the sky background. Finally, the QSO continuum model was subtracted from this residual data cube.

4.2. Lyα Line Measurements

We searched for emission lines in the processed data cubes in 1000 km s^{-1} velocity slices centered at the wavelength of the DLA. To avoid the wings of the DLA, narrower velocity slices had to be used at the position of the QSO. Depending on the target, values between 500 km s^{-1} and 1000 km s^{-1} were used. Then, Gaussian emission lines were fitted in these velocity slices for every spaxel. The free parameters of the fit were the line centroid, the peak flux density, and the line width. This step was repeated 500 times on 500 error-perturbed spectra for every spaxel, which yielded a line flux distribution for every spaxel around the expected redshifted Lyα wavelength. The mean and the standard deviation of each distribution were taken as the measured line flux and line flux error ($F_{Ly\alpha}$ and $eF_{Ly\alpha}$) at every spaxel.

To associate a S/N to an emission line, we quantified the line flux distribution across the data cube around the expected redshifted Lyα wavelength. To do this, we first masked all emission lines with $\geqslant 2\sigma$ significance, and then added back the background and the QSO emission. We then produced 200 error-perturbed data cubes for every target and carried out background and QSO subtraction for each such cube. Line fluxes were then measured across these data cubes, yielding a false-positive line flux distribution for every spaxel around the redshifted Lyα wavelength (see Figure 3). The line fluxes of the error-perturbed data cubes were then rank ordered to obtain the correspondence between line flux and percentile. This correspondence was used to assign a S/N to every Lyα line flux measurement in the original data cube.

We found that $S/N_{Ly\alpha} = 5$ effectively separates significant and spurious detections in the KCWI data cubes. For all significant detections, we recomputed the line fluxes to ensure that we account for spatially extended sources. To this end, we coadded the spectra of all the spaxels adjacent to the spaxel containing the detection. Our line flux fitting algorithm (see above) was then used to estimate the total line flux in the coadded spectrum. The Lyα line fluxes and errors reported throughout the rest of the paper correspond to the values measured in the coadded spectra. The S/N was not recalculated, i.e., the values of $S/N_{Ly\alpha}$ reported throughout were measured in the spaxel showing the highest significance.

For targets with no significant detections, we characterized our line flux sensitivity within the KCWI field of view. To this end, we inserted 10,000 emission lines with varying line fluxes and profile shapes in randomized locations within each data cube. The shapes of the simulated emission lines were chosen to be Gaussian, with 1σ widths between 150 and 225 km s^{-1}. The line flux at which we were able to recover 95% of the lines with at least $S/N_{Ly\alpha} = 5$ was defined as our Lyα sensitivity limit (Figure 3).

Inspection of the data cubes revealed 14 sources of continuum emission. With no line emission at the expected redshifted Lyα wavelength, these sources are most likely foreground interlopers at redshifts lower than that of the DLA. Of the 14 sources, seven are bright at the redshifted Lyα

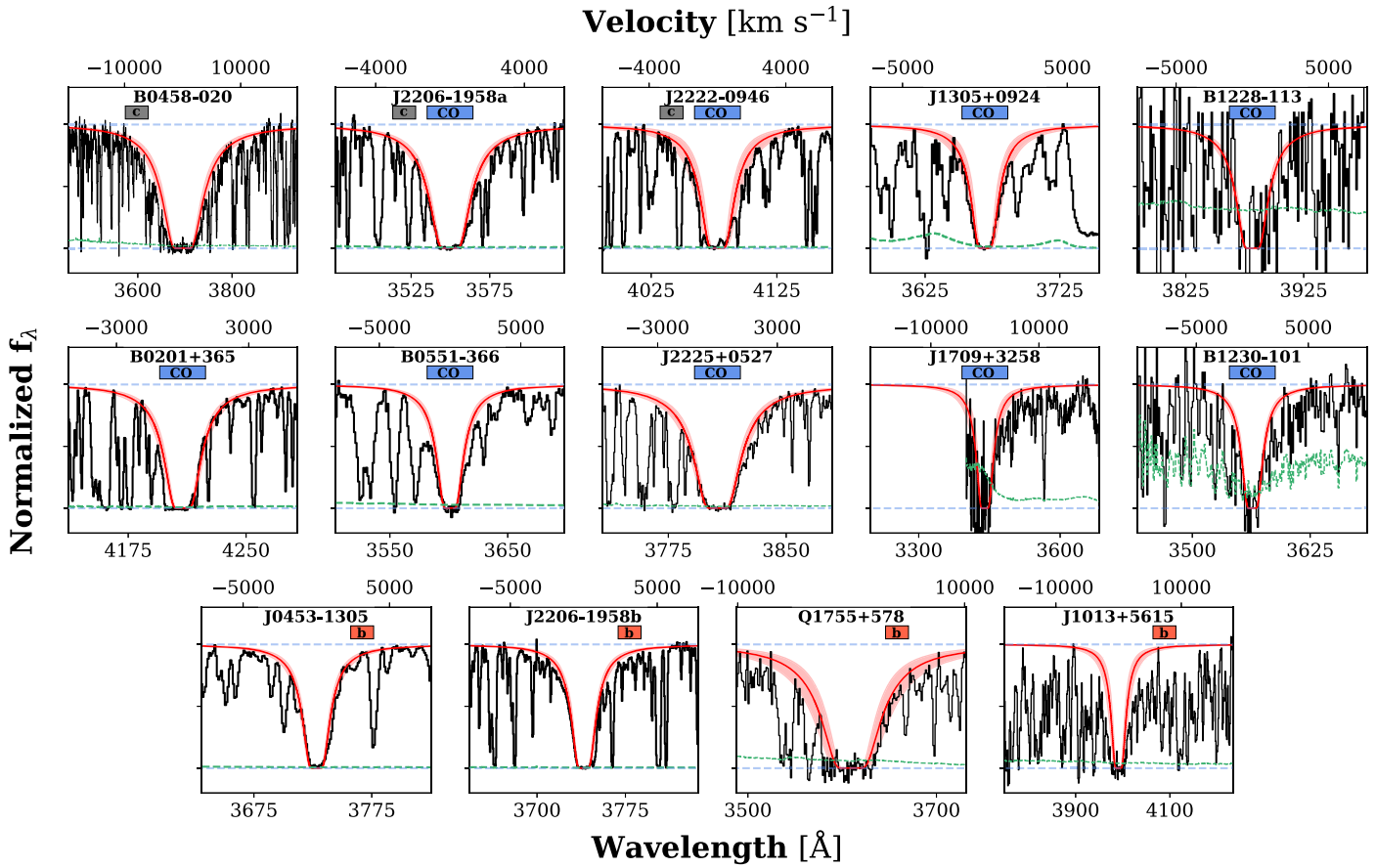

Figure 2. Spatially integrated KCWI spectra for the 14 QSOs after continuum normalization. Every panel shows the spectrum (continuous black lines) and the error (dashed green lines) at the wavelength of the DLA. The red lines and shaded regions show the best solution and the error on the DLA fits that were used to determine the redshifts and H I column densities of the absorbers (Rafelski et al. 2012, 2014). The symbols underneath the name of the target denote the sample the DLAs belong to. We note that the DLA along the J1305+0924 sightline is proximate, i.e., the DLA is within 5000 km s^{-1} of the Lyα emission from the QSO.

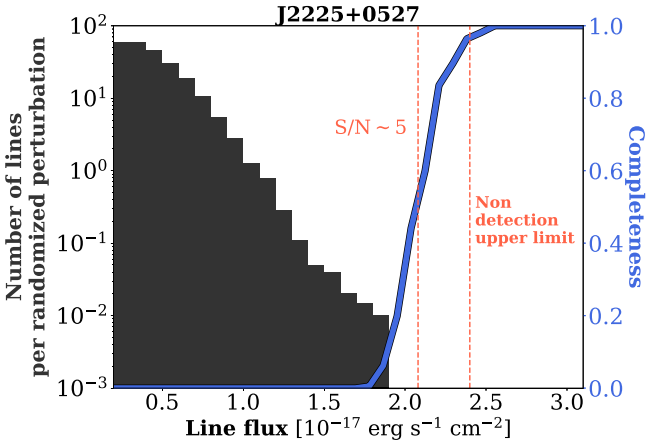

Figure 3. Example of the output from our line detection routine for the DLA along QSO J2225+0527. Plotted are all false positives (black histogram, left y-axis) and our completeness (blue filled line, right y-axis). These quantities are shown at the wavelength of the DLA absorption and after collapsing over the spatial component. The false-positive histogram was obtained by running our line detection code on error-perturbed spectra. The completeness curve corresponds to the fraction of planted lines that we were able to measure with at least $S/N_{Ly\alpha} = 5$ as a function of line flux. The detection threshold and nondetection upper limit (completeness ~95%) are shown as red dashed lines.

wavelength, and we therefore highlight them in white boxes in figures throughout the paper.

We also performed a search for Lyα nebulae around the QSOs of our sample. This search could not be performed for four of the 13 QSOs (J2222-0946, B1228-113, B0201+365, and J1013+5615) because their Lyα emission was redshifted out of the spectral coverage of KCWI. Out of the remaining nine QSOs, we found evidence for spatially extended Lyα emission in two cases. The emission extends over at least 70 kpc around QSO J2225+0527 and over ≈40 kpc around QSO J0453-1305. The two Lyα nebulae are shown in Figure 4. In passing, we note that the spatial resolution of our observations at the redshift of the QSO is typically ≈14 kpc FWHM, implying that the Lyα emission extends over at least two spatial beams in both cases. Similarly to Herenz et al. (2015), we find that the Lyα nebulae incidence rate (≈20%) is lower than what is typically obtained in dedicated searches (50%–70%; e.g., Roche et al. 2014; Arrigoni Battaia et al. 2016; Farina et al. 2017; Arrigoni Battaia et al. 2019; Cai et al. 2019; Farina et al. 2019; O'Sullivan et al. 2020), although we are limited by small-number statistics.

5. Results

We detected 5 statistically significant Lyα emission lines in the fields of 4 of the 14 DLAs in our sample—toward B0458-020 ($z \approx 2.041$), J2206-1958 ($z \approx 1.923$), J2222-0946 ($z \approx 2.357$), and B0551-366 ($z \approx 1.963$ and $z \approx 1.957$). The spatially integrated Lyα emission spectra and the velocity-integrated Lyα images for these detections are plotted in Figure 5. Three of these DLAs belong to our Lyα control sample, i.e., these three Lyα emitters had been earlier identified

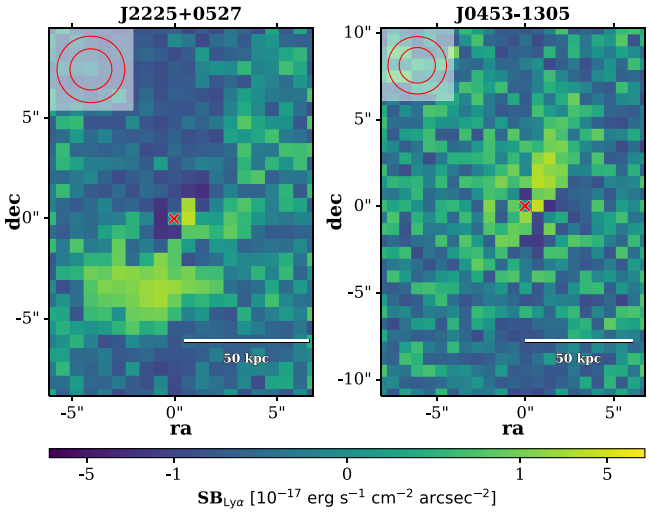

Figure 4. Two spatially extended Lyα nebulae around QSO J2225+0527 and QSO J0453-1305. Plotted is the surface brightness in Lyα after subtraction of the QSO continuum. The sizes of the point spread functions (1σ and 2σ contours) are shown in the top left corners. The spatial extension of the emission extends over at least two spatial beams, with the structure in QSO J2225+0527 extending over at least 70 kpc and the nebulae around QSO J0453-1305 apparent out to at least 40 kpc.

via slit spectroscopy (Møller et al. 2002, 2004; Fynbo et al. 2010). We also note that two of these control DLAs, toward J2222-0946 and J2206-1958, are part of the CO sample. No CO emission was detected by Kanekar et al. (2020).

The fourth and fifth Lyα detections are toward B0551-366. This DLA is part of the CO sample, featuring a CO detection. The Lyα emitters are at impact parameters of 53 kpc and 70 kpc (see Figure 5), which are much larger than the impact parameter of the CO emitter in this system (15 kpc). Remarkably, the Lyα redshift of the galaxy that is $\approx$53 kpc away from the DLA sightline is in excellent agreement with the DLA redshift ($\lesssim$100 km s^{-1}; Figure 5).

None of the six DLAs with significant or tentative CO detections show any evidence for Lyα emission within 50 kpc of the DLA (see Figures 5 and 6). In passing, we note that the tentative CO detection at $z = 1.83$ toward J1709+3258 is just outside the field of view of our KCWI coverage. Finally, of the four DLAs in the "blind" sample, we obtained a tentative (S/N$_{Ly\alpha} \approx 4$) detection of Lyα emission at $z \approx 2.067$ toward J0453-1305. The Lyα emission spectrum and image for this tentative detection are shown in the last column of Figure 5. Our detections and nondetections of Lyα emission are summarized in Table 2.

The Lyα emitter associated with the $z \approx 2.0395$ DLA along the sightline to B0458-020 was first reported by Møller et al. (2004; see also Krogager et al. 2017). The galaxy was found to have a Lyα flux of $(6.4 \pm 1.3) \times 10^{-17}$ erg s^{-1} cm^{-2} at an impact parameter of 2.7 ± 0.3 kpc to the DLA sightline (Krogager et al. 2017). For the $z \approx 2.3543$ DLA along J2222-0946, the Lyα emitter was characterized in Fynbo et al. (2010) and Krogager et al. (2013), with a Lyα flux of $(14.3 \pm 0.3) \times 10^{-17}$ erg s^{-1} cm^{-2} at an impact parameter of 6.3 ± 0.3 kpc (Krogager et al. 2017). Finally, the galaxy associated with the $z \approx 1.9200$ DLA toward J2206-1958 was found to have a Lyα flux of $(2.6 \pm 0.3) \times 10^{-16}$ erg s^{-1} cm^{-2} at an impact parameter of $\approx$5.8 kpc by Møller et al. (2002). In all three cases, our measurements for the Lyα fluxes and impact parameters of the Lyα emitters (see Table 2) are consistent (within $\approx 1.5\sigma$ significance) with the above measurements from the literature.

For the new Lyα detections, the Lyα emitters along the sightline toward B0551-366 have fluxes of $(12 \pm 5) \times 10^{-17}$ erg s^{-1} cm^{-2} for the source at an impact parameter of $\approx$53 kpc, and of $(17 \pm 6) \times 10^{-17}$ erg s^{-1} cm^{-2} for the source at $b \approx 70$ kpc. For the tentative Lyα detection associated with the $z \approx 2.0666$ DLA toward J0453-1305, we obtain a line flux of $(4.2 \pm 3) \times 10^{-17}$ erg s^{-1} cm^{-2} at an impact parameter of 6 ± 6 kpc. We obtain S/N$_{Ly\alpha} \approx 4$ for this emitter, which was determined via simulations of the data cubes. It should be noted that the error on the flux is dominated by the error in the flux scale.

Figure 7 shows the results of our Lyα searches from galaxies associated with DLAs at $z \approx 2$, with Lyα luminosity plotted as a function of [A] DLA metallicity and [B] H I column density. Lyα detections are shown as filled black circles and Lyα nondetections (and 5σ upper limits on the Lyα luminosity) as downward-pointing arrows. The gray shaded region shows the expected Lyα luminosity for a given galaxy metallicity, assuming the observed stellar mass–metallicity relation for star-forming galaxies at $z \approx 2$ (Erb et al. 2006) and the galaxy main-sequence relation at $z \approx 2$ (with an assumed spread of 0.35 dex; Whitaker et al. 2014; Mérida et al. 2023). After using the Hα SFR calibration of Kennicutt & Evans (2012), a dust-free Lyα to Hα luminosity ratio of 8.7, and a Chabrier (2003) initial mass function (e.g., Matthee et al. 2016; Oyarzún et al. 2017; Sobral & Matthee 2019), the above relations were used to determine the expected Hα line luminosity as a function of galaxy metallicity. Similarly, also shown in Figure 7 (orange) is the expected Lyα luminosity if one takes the mass–metallicity relation of DLA absorption-selected galaxies with a scatter of 0.38 dex (Møller et al. 2013; Christensen et al. 2014).

It is clear from Figure 7(A) that most of our Lyα detections arise in the fields of DLAs with relatively low absorption metallicities. Indeed, only one of the nine DLAs with [M/H] > -0.3 shows a detection of Lyα emission, while four of the five DLAs with [M/H] $\leqslant -0.5$ show either clear or tentative detections of Lyα emission. Further, the figure shows that many of the Lyα detections of our survey lie close to the gray shaded region, i.e., are in reasonable agreement with the expected Lyα line luminosity, despite the strong assumptions of (1) a dust-free Lyα to Hα luminosity ratio and (2) absorption metallicity equal to emission metallicity. This is seen to be the case for all DLAs with [M/H] $\lesssim -0.5$. However, for the higher-metallicity DLAs, with [M/H] > -0.3, most of the upper limits on the Lyα line luminosity are in clear conflict with the expected line luminosity, typically lying more than an order of magnitude below the expected values. The most likely cause of this discrepancy is significant dust extinction of the Lyα line in the galaxies in the fields of the highest-metallicity DLAs at $z \approx 2$ (more in Section 6).

While no clear trend is apparent in Figure 7(B), which plots the Lyα line luminosity versus DLA H I column density, we cannot yet conclude that Lyα luminosity is not correlated with $N_{\rm H\,I}$ for DLAs at $z \approx 2$. Apparent in this figure is that the coverage toward $N_{\rm H\,I} > 10^{21}$ cm^{-2} in current surveys is limited. While the survey by Krogager et al. (2017) included some high-$N_{\rm H\,I}$ DLAs, the associated galaxies are biased toward low impact parameters due to the slit-based nature of their search. Therefore, more data are needed in order to

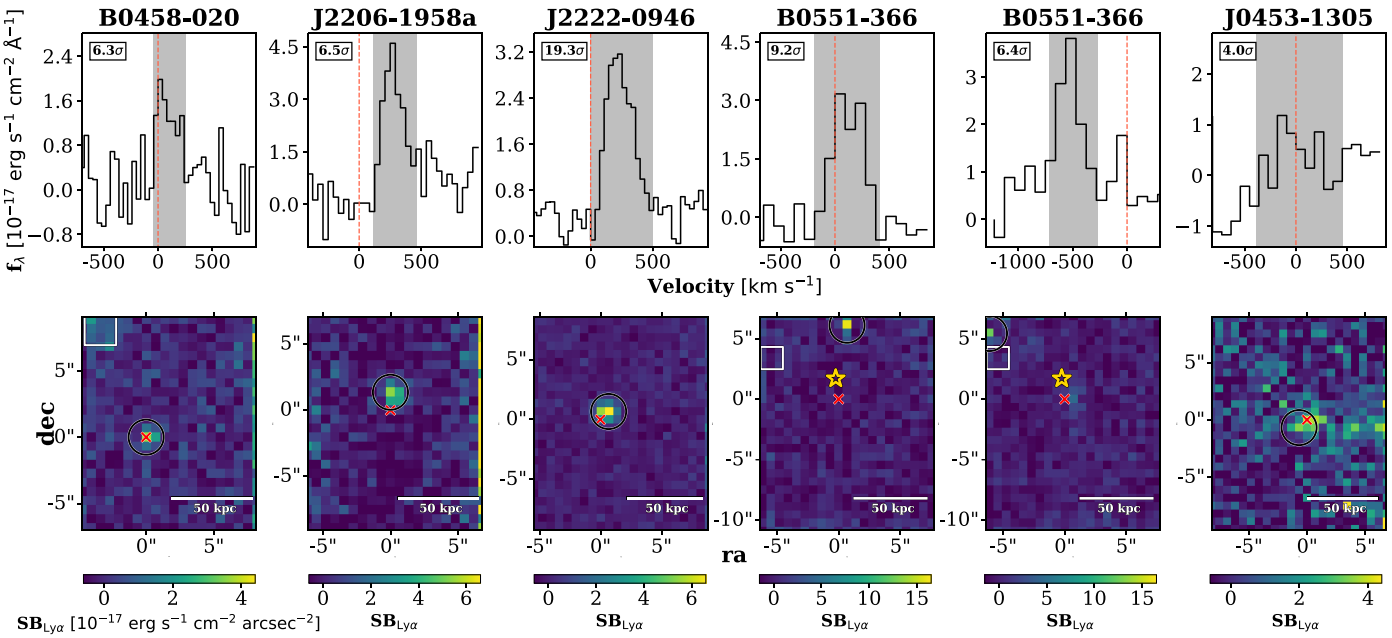

Figure 5. Visualization of our line search for the six Lyα detections. The six columns correspond to the six Lyα emission lines. Top: spatially integrated Lyα emission after subtraction of the QSO continuum. The red dashed line shows the Lyα absorption wavelength. The Lyα emitters along B0458-020, J2206-1958, and J2222-0946 are part of our control sample, i.e., they were originally detected in searches for Lyα emitters around DLAs at low impact parameters. Two more Lyα emitters at $b \approx 53$ kpc and $b \approx 70$ kpc away from DLA B0551-366 were also found. This DLA also has a CO emitter at $b \approx 15$ kpc. The field showing a tentative detection—J0453-1305—belongs in the blind sample, i.e., it has not been a target in any CO or Lyα searches. Bottom: integrated flux of the spectrum in the KCWI cubes centered at the redshifted Lyα absorption and within a window of width equal to the emission line. The symbols show the position of the QSO (red cross), Lyα emission (circles), CO emitter (yellow star), and interlopers (white squares).

determine how $N_{\rm H\,I}$ and Lyα luminosity are related at these redshifts.

The two panels of Figure 8 show (A) the DLA metallicity [M/H], and (B) the DLA H I column density, plotted against galaxy impact parameter for our six detections of Lyα emission at $z \approx 2$. Besides these Lyα detections, we have included the six DLA galaxies identified in ALMA and NOEMA CO searches at $z \approx 1.8$–2.6 (Kanekar et al. 2020; Kaur et al. 2022a) and the five Lyα detections at similar redshifts obtained via slit spectroscopy in the literature (Krogager et al. 2017).

Figure 8(A) shows that there are galaxies over a wide range of impact parameters (≈6–100 kpc) in the fields of high-metallicity ([M/H] $\gtrsim -0.7$) DLAs. This suggests that high-metallicity DLAs at $z \approx 2$ may arise from both galaxy disks and extended gas in the environment of massive galaxies, with the circumgalactic medium (CGM) being enriched due to galactic outflows. Conversely, the DLA galaxies associated with low-metallicity ([M/H] $\lesssim -1$) DLAs are seen to have low impact parameters ($b \lesssim 10$ kpc; although we note that there are only four galaxies in this category). Figure 8(B) plots the H I column density against impact parameter for the above sample of Lyα-detected and CO-detected galaxies. It is clear that similar H I column densities, $\approx 10^{20.5}$–10^{21} cm^{-2}, are found in DLAs over a wide range of galaxy impact parameters, ≈5–100 kpc.

Finally, Figure 9 compares our results to those obtained from IFU- and slit-based Lyα searches in the fields of high-redshift DLAs in the literature. Included in this figure are the Lyα detections and nondetections from our work, four slit-based detections around four DLAs at $z \approx 2$ (Krogager et al. 2017), five Lyα emitters around three DLAs at $z \gtrsim 3$ (Fumagalli et al. 2017; Mackenzie et al. 2019), a Lyα emitter at $z \approx 3$ (Joshi et al. 2021), three Lyα emitters around a $z \approx 2.4$ DLA (Nielsen et al. 2022), and 23 Lyα emitters around nine DLAs at $z \approx 3$–3.8 (Lofthouse et al. 2023). We emphasize that the Lyα detections shown in this figure span a wide range of impact parameters, and that these previous observations have shown that DLAs can arise from galaxy groups (e.g., Fynbo et al. 2018). It is therefore likely that some of the galaxies at large impact parameter are companion galaxies of the galaxy that gives rise to the DLA absorption (e.g., Mackenzie et al. 2019; Lofthouse et al. 2023). This is consistent with the results from hydrodynamical simulations (e.g., Rahmati & Schaye 2014; Rhodin et al. 2019).

The different panels in Figure 9 show how the Lyα luminosity depends on (A) DLA metallicity, (B) H I column density, (C) redshift, and (D) impact parameter. We note that the DLAs with searches for Lyα emission at $z \gtrsim 3$ typically have low metallicities, [M/H] $\lesssim -1$, while most of our KCWI searches are in the fields of high-metallicity DLAs. The luminosity of our upper limits decreases with redshift, reflecting how the spectral S/N decreases substantially for $z < 2$ as a result of the degradation in sensitivity of KCWI blueward of 3700 Å.

Figure 8(D) might hint that DLAs at $z \gtrsim 3$ are more often associated with galaxy groups (with $\geqslant 3$ galaxies) than DLAs at $z \approx 2$. Four out of 13 DLAs at $z \gtrsim 3$ feature at least three Lyα emitters in their fields (Mackenzie et al. 2019; Lofthouse et al. 2023), while only a single DLA at $z \approx 2$ (out of 15) has $\geqslant 3$ associated Lyα emitters (Nielsen et al. 2022). However, this apparent difference could be driven by variations in survey design. There is a significant difference between the fields of view of KCWI (≈170 kpc × 277 kpc) and VLT-MUSE (≈450 kpc × 450 kpc), the instrument used by the surveys of Mackenzie et al. (2019) and Lofthouse et al. (2023). This

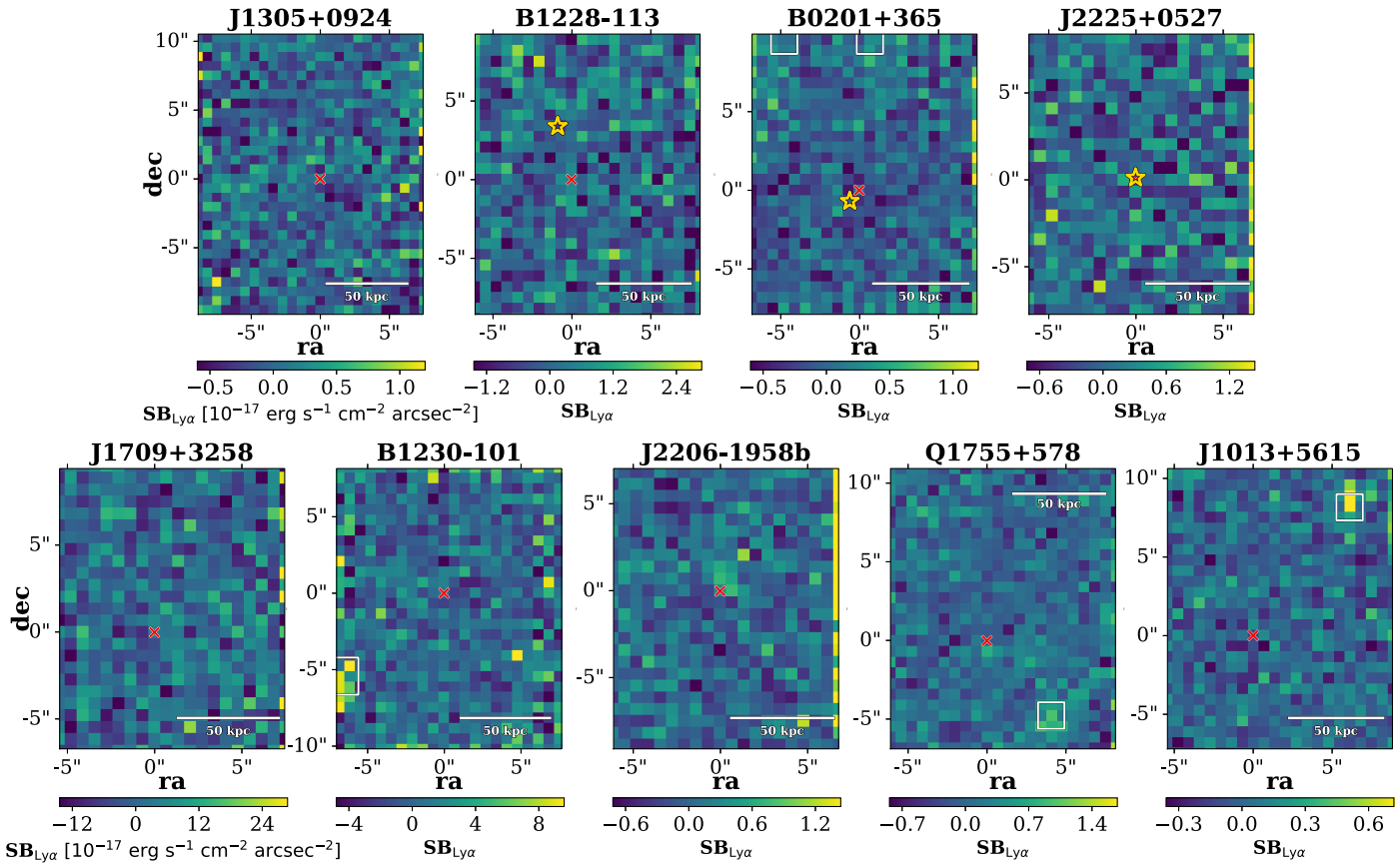

Figure 6. KCWI cubes for all the Lyα nondetections. Shown is the integrated flux of the spectrum in the KCWI cubes centered at the redshifted Lyα absorption and within a window of width 350 km s^{-1}. The position of the QSOs are shown with a red cross and the location of the CO-emitters is shown with yellow stars. Some fields show significant interloper emission that is spatially offset from the QSO (white squares).

difference becomes even greater when we consider that our effective field of view is $\approx$170 kpc $\times$ 130 kpc (Section 3), which can be even smaller if the QSO is not perfectly centered (Figures 5 and 6). Difference in sensitivities between the surveys could also play a role, with Mackenzie et al. (2019) and Lofthouse et al. (2023) achieving lower Lyα luminosities than our analysis (Figure 9). Thus, it is clear that searches with wider fields of view and higher sensitivities at $z \approx 2$ are needed in order to test for possible redshift evolution in DLA environments.

6. Discussion

Our KCWI survey has yielded new detections of Lyα emission along the DLA sightline toward B0551-366, a tentative detection from the DLA field toward J0453-1305, and recoveries of all three known Lyα detections from the control sample. Restricting to the new (i.e., noncontrol) searches, we have obtained definite Lyα detections along only a single DLA sightline out of 11, with nine of the target DLAs having high metallicities ([M/H] > -0.3). We also do not detect Lyα emission from any of the four CO-emitting galaxies in the sample, although one of these sightlines (B0551-366) shows Lyα emission from two other galaxies within $\pm$500 km s^{-1} of the CO and DLA redshifts. We discuss in this section the implications of these results, in conjunction with those from surveys from the literature, to gain insights into the nature of the galaxies associated with high-metallicity DLAs at $z \approx 2$.

6.1. The Galaxies Associated with High-metallicity DLAs at z $\approx$2 Are Not Typical Lyα Emitters

The left panel of Figure 7 shows that the Lyα luminosity of galaxies in the field of high-metallicity ([M/H] $\geqslant -0.3$) DLAs at $z \approx 2$ lies well below the predicted Lyα luminosity of emission-selected galaxies at similar redshifts. We emphasize that the predicted Lyα luminosity has been obtained with the assumption of a dust-free Lyα-to-Hα ratio. There are two possibilities to explain this discrepancy: (1) the galaxies associated with high-metallicity DLAs have low stellar masses, and hence intrinsic Lyα luminosities below our detection threshold, or (2) the assumption of a dust-free Lyα-to-Hα ratio breaks down, with the galaxies associated in high-metallicity DLA fields being typically massive, dusty galaxies with high production and high absorption of Lyα photons. In this section, we consider the first possibility by turning to two different methods of estimating the luminosities of low-mass ($M_* \approx 10^8\,M_\odot$) galaxies. As shown in Oyarzún et al. (2016, 2017), galaxies of this stellar mass have Lyα equivalent widths (50–200 Å; Charlot & Fall 1993) and escape fractions ($\approx$1; Laursen et al. 2009) that are typical of dust-free interstellar media.

In the first approach, we will assume that any undetected galaxies belong to the star formation main sequence at $z \approx 2$. The slope and scatter of the main sequence at $z \approx 2$ has been measured down to a stellar mass of $M_* \approx 10^8\,M_\odot$ by Mérida et al. (2023). At this mass, the SFR distribution has an average of $\log(\mathrm{SFR}/M_\odot\,\mathrm{yr}^{-1}) \sim 0$ and a scatter of

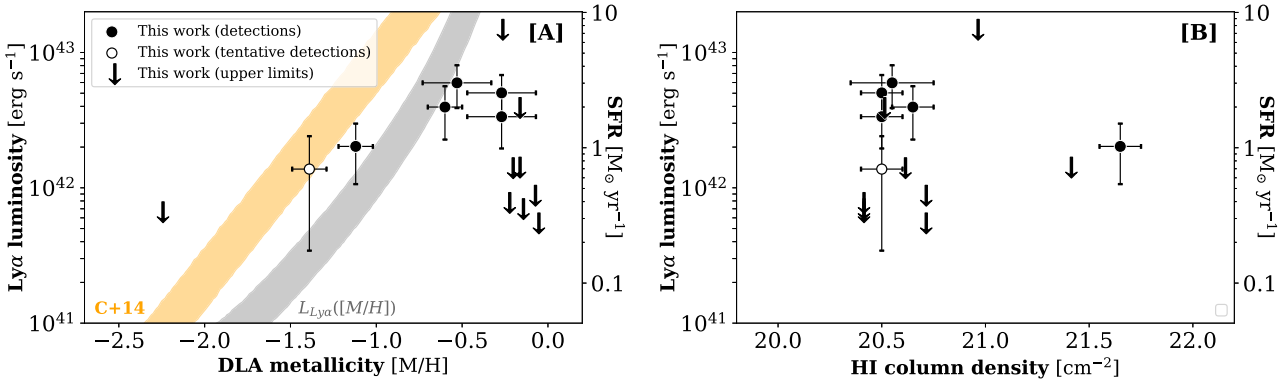

Figure 7. The dependence of the Lyα luminosity of the galaxies in the fields of DLAs at $z \approx 2$ on (A) the DLA metallicity and (B) the DLA H I column density. Detections of Lyα emission with $\geqslant 5\sigma$ significance are plotted as black circles, tentative (4σ–5σ) detections as open circles, and Lyα nondetections (i.e., 5σ upper limits to the Lyα line luminosity) as downward-pointing arrows. The gray shaded region in panel (A) indicates the expected Lyα luminosity as a function of galaxy metallicity, which was obtained by combining the star-forming main-sequence relation at $z \approx 2$ (Whitaker et al. 2014) with the observed stellar mass–metallicity relation for emission-selected galaxies at $z \approx 2$ (Erb et al. 2006). The orange shaded region in this panel shows the expected Lyα luminosity as a function of DLA metallicity by combining the same star-forming main-sequence relation at $z \approx 2$ with the mass–metallicity relation for H I-selected galaxies at $z \approx 2$ (Christensen et al. 2014). While a few of the Lyα luminosities measured in our survey lie on or close to the gray band at intermediate metallicities, it is clear that the upper limits to the Lyα luminosity for the highest-metallicity DLAs are more than an order of magnitude below this band.

$\Delta\log(\mathrm{SFR}/M_\odot\ \mathrm{yr}^{-1}) \sim 0.35$ dex. Following the approach of Section 5, this SFR can be converted into a Lyα luminosity $L_{\mathrm{Ly}\alpha}$ by assuming a dust-free Lyα-to-Hα ratio and the Hα SFR calibration for a Chabrier IMF. In the resulting $L_{\mathrm{Ly}\alpha}$ distribution, the probability that a galaxy has a Lyα luminosity lower than our upper limits is $p \approx 20\%$ (on average) for the eight high-metallicity DLAs with tight upper limits on the Lyα luminosity (i.e., J1305+0924, B1228-113, B0201+365, J2225+0527, B1230-101, Q1755+578, and J1013+5615). Thus, the probability that all of these DLAs feature typical Lyα emitters with $M_* \approx 10^8\,M_\odot$ within $\approx$50 kpc of the QSO sightline is $p \lesssim 10^{-5}$.

Alternatively, we can turn to the rest-frame Lyα equivalent width ($\mathrm{EW}_{\mathrm{Ly}\alpha}$) instead of the Ly$\alpha$ luminosity. This quantity is defined as

$$\mathrm{EW}_{\mathrm{Ly}\alpha} = \frac{F_{\mathrm{Ly}\alpha}}{f_\lambda}\frac{1}{(1+z)}, \tag{3}$$

where $F_{\mathrm{Ly}\alpha}$ is the Lyα line flux and f_λ is the rest-frame flux density of the galaxy in the near-UV. We note that the $\mathrm{EW}_{\mathrm{Ly}\alpha}$ is a convenient metric because the $\mathrm{EW}_{\mathrm{Ly}\alpha}$ distribution of high-redshift galaxies has been thoroughly quantified in the literature (e.g., Gronwall et al. 2007; Treu et al. 2012; Jiang et al. 2013).

For low-mass galaxies with $M_* \approx 10^8\,M_\odot$ and $\log(\mathrm{SFR}/M_\odot\ \mathrm{yr}^{-1}) \sim 0$, the rest-frame near-UV flux densities are typically in the range $f_\lambda \sim (1\text{–}10) \times 10^{-19}$ erg s^{-1} cm^{-2} Å^{-1} (e.g., Skelton et al. 2014). With f_λ in hand along with the upper limits on the Lyα line flux density, we obtain typical upper limits to the rest-frame equivalent width of $\mathrm{EW}_{\mathrm{Ly}\alpha} \lesssim 30$Å within $\approx$50 kpc of the eight high-metallicity DLAs in our sample.

The expected Lyα detection rate of our observations can now be estimated from the known $\mathrm{EW}_{\mathrm{Ly}\alpha}$ distribution of galaxies at $z \approx 2$. A number of authors have concluded that the $\mathrm{EW}_{\mathrm{Ly}\alpha}$ distribution at this redshift is well fitted by an exponential profile with a scale length of $\mathrm{EW}_0 \approx 50$Å (e.g., Nilsson et al. 2009; Guaita et al. 2010; Mawatari et al. 2012; Ciardullo et al. 2014). Knowing that the $\mathrm{EW}_{\mathrm{Ly}\alpha}$ distribution accounts for $\approx$80% of the galaxy population at $M_* \lesssim 10^9\,M_\odot$ ($z \sim 4$; Oyarzún et al. 2016), integration of this probability distribution from $\mathrm{EW}_{\mathrm{Ly}\alpha} = 0$ up to our $\mathrm{EW}_{\mathrm{Ly}\alpha}$ limits yields $\approx$80% of the probability that an $M_* \approx 10^8\,M_\odot$ galaxy was not detected by our survey. This results in total probabilities of $\approx$40% for each of our eight nondetections, yielding a probability of $p \approx 2 \times 10^{-4}$ that all eight of these high-metallicity DLAs have low stellar mass galaxies within $\approx$50 kpc of the QSO sightline.

These results indicate that the majority of the galaxies associated with high-metallicity DLAs at $z \approx 2$ are not unobscured galaxies with low stellar masses, i.e., $M_* \approx 10^8\,M_\odot$. In fact, characterization of the galaxies associated with high-metallicity DLAs at $z \approx 2$ has yielded stellar masses exceeding $10^{10}\,M_\odot$ (e.g., Fynbo et al. 2013).

6.2. The Galaxies Associated with High-metallicity DLAs at z ≈ 2 Are Probably Massive and Dusty

A galaxy can also remain undetected in Lyα emission if it has a low Lyα escape fraction. This would typically arise because of Lyα photon absorption by dust grains, as indicated by several radiative transfer simulations (e.g., Verhamme et al. 2008; Laursen et al. 2009). This has been argued to be the reason for why high-redshift galaxies with redder UV slopes show lower Lyα emission equivalent widths (e.g., Blanc et al. 2011; Hayes et al. 2011; Atek et al. 2014; Oyarzún et al. 2017). At the same time, the escape of Lyα photons is affected by the scattering of radiation by neutral gas, such that the structure and kinematics of the interstellar and circumgalactic media of galaxies can shape the Lyα line profile (e.g., Verhamme et al. 2006).

The dependence of the Lyα escape fraction on the neutral gas covering fraction and dust extinction has implications for the use of Lyα as a galaxy tracer. Star-forming galaxies with higher neutral gas masses and dust extinctions tend to have higher stellar masses (e.g., Reddy et al. 2006; Finlator et al. 2007; Tacconi et al. 2020), implying that Lyα emission might not be a good tracer of the high stellar mass end of the star-forming galaxy population. In agreement with this picture, the equivalent width of the Lyα emission line in high-redshift galaxies has been found to anticorrelate with the stellar mass (e.g., Oyarzún et al. 2016).

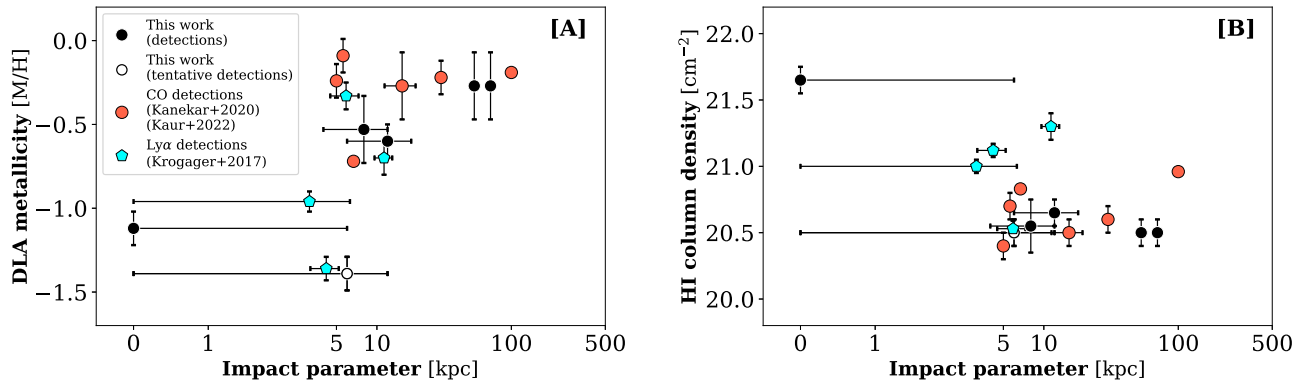

Figure 8. (A) DLA metallicity and (B) DLA H I column density plotted against galaxy impact parameter for DLA galaxies at $z \approx 2$. As in Figure 7, plotted are detections (black circles) and tentative detections (open circles). Also included are the slit spectroscopy measurements from Krogager et al. (2017) and the CO emission measurements from Kanekar et al. (2020) and Kaur et al. (2022a, 2022b).

Instead, massive galaxies tend to be bright in mm or submm emission lines (e.g., CO or [C II] 158 μm), whose luminosity correlates with the total molecular gas mass (i.e., with the stellar mass). Thus, it is not surprising that the CO rotational lines have been particularly useful in identifying the galaxies associated with the highest-metallicity DLAs at $z \approx 2$ (Kanekar et al. 2020; Kaur et al. 2022b). Kaur et al. (2022b) find that the detection rate of CO emission is strongly dependent on DLA metallicity, with a CO detection rate of ≈50% for $[M/H] > -0.3$, and a far lower CO detection rate at lower metallicities.

The suggestion that Lyα and CO emission are efficient at identifying the galaxies associated with DLAs of different metallicities is supported by Figures 8(A) and 9. Galaxies detected through Lyα emission tend to be brighter for DLAs with $[M/H] \lesssim -1.0$. This is likely to arise due to dust obscuration effects, with higher-metallicity galaxies also having high dust contents that impede the escape of Lyα photons. Conversely, the requirements of both a high molecular gas mass and a low CO-to-H_2 conversion factor imply that searches for CO emission favor the identification of the high-mass galaxies associated with high-metallicity DLAs. In line with the detection of dusty galaxies in association with high-metallicity DLAs, it is plausible that the majority of these absorbers arise from massive, dusty galaxies that are faint in Lyα emission (e.g., Fynbo et al. 2013).

In this context, it is interesting to consider why some of the highest-metallicity DLAs show no evidence of CO emission from associated galaxies (Kanekar et al. 2020; Kaur et al. 2022b). This is likely a result of the sensitivities of the current ALMA and NOEMA searches, which typically yield upper limits of ≈ 1–$5 \times 10^{10}\,M_\odot$ on the molecular gas masses of these galaxies (Kanekar et al. 2020; Kaur et al. 2022b). These upper limits are not necessarily constraining, and thus current CO nondetections do not rule out the presence of massive galaxies in the DLA fields.

Given that high-mass galaxies associated with high-metallicity DLAs may be missed in searches for both Lyα and CO emission, turning to different diagnostics emerges as a valid strategy. The best probes to identify such galaxies are likely to be Hα, [O III]λ5007, and [C II] 158 μm emission. The Hα and [O III]λ5007 lines are less affected by dust obscuration than Lyα, and they can be used to probe galaxies in the stellar mass range $M_* = 10^8$–$10^{10}\,M_\odot$ (e.g., Péroux et al. 2011, 2012; Jorgenson & Wolfe 2014; Wang et al. 2015). While this line is difficult to access from the ground for galaxies at $z > 2$, the James Webb Space Telescope should allow the Hα-based identification of large samples of high-mass DLA galaxies out to $z \sim 4$. Similarly, while the [C II] 158 μm emission from galaxies at $z \approx 2$ lies at very high frequencies (>600 GHz), it should be possible to use ALMA [C II] 158 μm searches to identify such galaxies.

6.3. Implications for the Nature of H I-selected Galaxies at High Redshift

Searches for the galaxies associated with DLAs at high redshift have made remarkable progress over the last few years, with more than 40 galaxies identified via Lyα, CO, or [C II] 158 μm searches (e.g., Fumagalli et al. 2017; Krogager et al. 2017; Neeleman et al. 2017, 2018; Mackenzie et al. 2019; Neeleman et al. 2019; Kanekar et al. 2020; Kaur et al. 2022b; Lofthouse et al. 2023). While we now have a large sample of H I-selected galaxies, the wide range of DLA redshifts ($z \approx 2$–4.5), DLA metallicities ([M/H] −2.5–0), and different selection techniques imply that it is not straightforward to draw conclusions about their nature. Here, we briefly summarize the current observational view of this population in order of increasing redshift.

First, the bulk of the H I-selected galaxies identified in slit-based Lyα searches at $z \approx 2$ lie at low impact parameters to the QSO sightline (e.g., Fynbo et al. 2013; Krogager et al. 2016, 2017; Joshi et al. 2021). This is not surprising, given that such searches are only sensitive toward galaxies at low impact parameters ($\lesssim$15 kpc). By design, these DLAs have high metallicities, i.e., between $[M/H] \approx -1.5$ and $[M/H] \approx -0.5$ (Krogager et al. 2017). The fraction of undetected galaxies and their H I metallicity distribution remains unclear.

At $z \approx 2$, our KCWI Lyα survey has revealed only 2–3 new H I-selected galaxies from a search in 11 DLA fields (excluding the control sample). Nine of our DLA targets have $[M/H] > -0.3$, of which only one showed a detection of Lyα emission. The KCWI survey is sensitive to galaxies with impact parameters $\lesssim$50 kpc.

At $z \approx 2$, ALMA and NOEMA CO searches have yielded six definite detections of H I-selected galaxies, all in the fields of DLAs with a metallicity of $[M/H] > -0.3$. (Kanekar et al. 2020; Kaur et al. 2022b). Five of the CO detections are at impact parameters of $\lesssim$30 kpc. The sixth system, toward

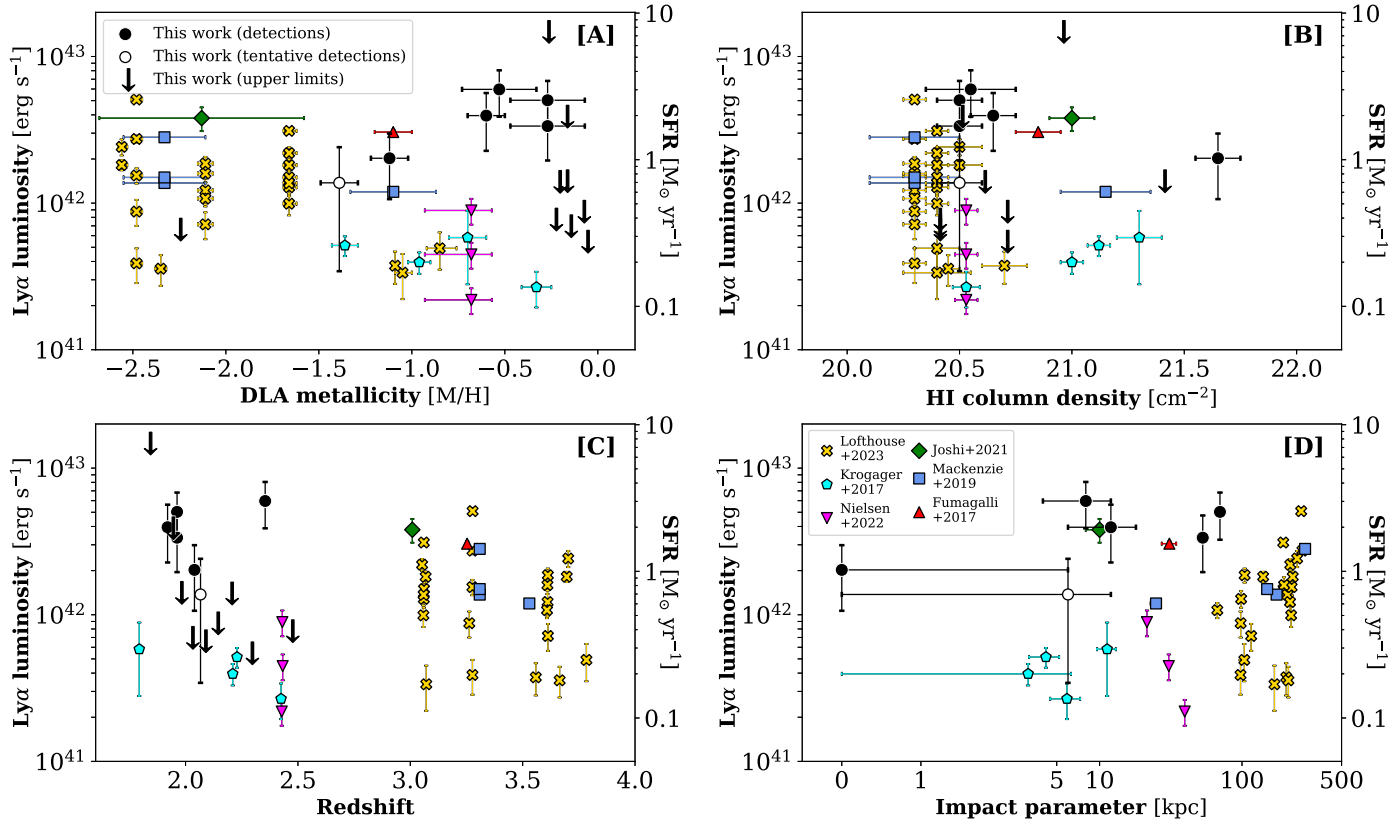

Figure 9. The results of our survey in the context of searches for Lyα emission from DLA fields at $z \gtrsim 2$ in the literature. The panels show the Lyα luminosity as a function of (A) DLA metallicity, (B) H I column density, (C) redshift, and (D) impact parameter. The results of our survey are shown as filled (detections) and open (tentative detections) circles, with upper limits to the Lyα luminosity indicated by the downward-pointing arrows. Plotted from the literature are the measurements of Fumagalli et al. (2017), Krogager et al. (2017), Mackenzie et al. (2019), Joshi et al. (2021), Nielsen et al. (2022), and Lofthouse et al. (2023). The corresponding symbols are indicated in (D).

Q0918+1636, has an impact parameter of ≈100 kpc; however, there is a galaxy at a lower impact parameter (≈16 kpc) to the QSO sightline that was identified in the optical (Fynbo et al. 2018). While the field of Q0918+1636 was not targeted by our survey, the DLA galaxy at an impact parameter of ≈16 kpc has been extensively characterized by Fynbo et al. (2011). The nondetection of Lyα emission from this galaxy down to fluxes of $\sim 5 \times 10^{-18}$ erg s^{-1} cm^{-2} is indicative of dust supression, especially given the high luminosity of its [O II] and [O III] emission (Fynbo et al. 2011).

At $z \approx 3$–3.5, Lyα spectroscopy with VLT/MUSE has yielded ≈28 Lyα detections of galaxies in DLA fields (Fumagalli et al. 2017; Mackenzie et al. 2019; Lofthouse et al. 2023). These DLAs have metallicities between [M/H] ≈ −2.5 and [M/H] ≈ −1. Almost all of the Lyα detections are at high impact parameters ($\gtrsim$100 kpc), and there are, in some cases, more than five galaxies identified in a single DLA field. Such galaxies would not have been detected either in the slit-based Lyα surveys (because of the field of view) or in the present KCWI survey (because of the sensitivity and/or field of view).

Finally, searches in [C II] 158 μm at $z \approx 3.8$–4.5 with ALMA have identified 10 galaxies in the fields of DLAs with [M/H] $\geqslant -1.3$ (e.g., Neeleman et al. 2017, 2019; Prochaska et al. 2019; Kaur et al. 2021). The impact parameters to the QSO sightline are large (15−50 kpc). Three of the DLA fields have more than two galaxies within ≈50 kpc of the QSO sightline.

Regarding the sizes of H I gas reservoirs, evidence indicates that they are quite extended, especially in low-redshift massive galaxies. Toward $z \approx 1.3$, Chowdhury et al. (2022a) have found that a spatial resolution of 90 kpc is needed in order to recover the total H I 21 cm emission of massive galaxies, indicating that the H I sizes of these galaxies are $\gtrsim$50 kpc at these redshifts. In the local Universe, the H I size has been found to correlate with the H I mass, with the diameter of H I disks exceeding 40 kpc in galaxies with H I masses $>10^{10}\,M_{\odot}$ (at an H I surface density of $1 M_{\odot}$ pc^{-2}, i.e., similar to the DLA column density threshold; e.g., Broeils & Rhee 1997; Wang et al. 2016). Thus, both direct measurements of H I 21 cm emission at $z \approx 1.3$ and the H I mass–size relation at $z \approx 0$ suggest that massive galaxies have large spatial extents in H I.

Chowdhury et al. (2022b) have concluded that H I dominates the baryonic mass of the disks of galaxies, with the H I mass exceeding the stellar mass and the molecular gas mass by factors of ≈4–5. Drawing a comparison with the CO detections of Kanekar et al. (2020) and Kaur et al. (2022b), the measurements by Chowdhury et al. (2022b) would imply an H I diameter of $\gtrsim$100 kpc at $z \approx 2$, even if we assume that the H I mass is only comparable to the molecular gas mass, ($\gtrsim 5 \times 10^{10}\,M_{\odot}$). With the H I-selected galaxies associated with high-metallicity ([M/H] $\gtrsim -0.5$) DLAs at $z \approx 2$ typically found at relatively low impact parameters ($\lesssim$30 kpc), it is plausible that high-metallicity DLAs at these redshifts arise from the disks of massive galaxies.

As concluded in Section 6.2, the low detection rate of these high-metallicity DLA fields in Lyα is likely due to dust obscuration effects in massive galaxies. Instead, less affected by dust obscuration (and brighter in Lyα) are expected to be galaxies of low-intermediate stellar masses (Section 6.1). Because of this, it is noteworthy how small the number of companion galaxies identified in Lyα is at $z \approx 2$. Only one of the H I-selected galaxies at low impact parameters (B00551-366) has been found to have companion galaxies within $\approx$50 kpc. This is likely to be due to relatively small fields of view of the current Lyα searches at $z \approx 2$.

The situation is somewhat different at $z \approx 3$–3.5, where Lyα searches have mostly identified galaxies at very large impact parameters ($\gtrsim$100 kpc) in the fields of DLAs with mostly low metallicities (between $[M/H] \approx -2.5$ and $[M/H] \approx -1$; Mackenzie et al. 2019; Lofthouse et al. 2023). If we assume that the low metallicity of the DLA is indicative of low dust obscuration, galaxies at low impact parameters would have only been missed if they were intrinsically underluminous. Under this assumption, DLAs at $z \approx 3$–3.5 with $[M/H] \lesssim -1$ arise from either low stellar mass galaxies at low impact parameters or from massive, dusty galaxies at large impact parameters. The large number of Lyα-emitting companions at distances of $\approx$100–200 kpc in a number of the fields is interesting, and suggests that the DLAs probed by these studies arise mostly in galaxy groups.

Finally, the impact parameters of the H I-selected galaxies identified in [C II] 158 μm searches at $z \gtrsim 4$ are $\approx$15–50 kpc (Neeleman et al. 2017, 2019). These [C II] 158 μm emitters are all associated with DLAs that have metallicities of $[M/H] \geqslant -1.35$, and while multiple galaxies have been identified in some fields, these are all at similar impact parameters (<50 kpc). Together, the high H I column densities ($\gtrsim 10^{21}$ cm^{-2}) and relatively large impact parameters hint that high-metallicity, high-$N_{\rm H\,I}$ DLAs at $z \gtrsim 4$ likely arise from H I clumps in the CGM of massive galaxies. This is consistent with numerical simulations that predict greater amounts of H I in the CGM of galaxies at $z \gtrsim 4$ than at lower redshifts (e.g., Stern et al. 2021).

7. Summary

We have used the integral field spectrograph KCWI on the Keck II telescope to carry out a search for Lyα emission in the fields of 14 DLAs at $z \approx 2$. Nine of the 14 targets have high metallicities ($[M/H] > -0.3$). Seven of the 14 fields have been searched for CO emission with ALMA or NOEMA, with four confirmed detections. Finally, three of the 14 DLAs are known Lyα emitters from the literature that were observed to quantify our Lyα detection capability (i.e., the control sample).

We detected Lyα emission with the expected strength from the three control-sample DLAs. For the remaining 11 targets, Lyα emission was detected from two galaxies in the field of the $z \approx 1.9622$ DLA toward B0551-366 at impact parameters of $\approx$50–70 kpc. Also in the field of B0551-366 is a massive CO-detected galaxy at an impact parameter of $\approx$15 kpc from the QSO sightline. This indicates that the Lyα emitters do not directly give rise to the DLA absorption. We find that the low Lyα detection rate in the fields of high-metallicity DLAs is likely a result of Lyα photon absorption by dust produced in massive and dusty galaxies.

We compared the results of our Lyα searches in DLA fields at $z \approx 2$ with those of CO searches at $z \approx 2$, Lyα searches at $z \approx 3$–3.5, and [C II] 158 μm searches at $z \approx 4$. The impact parameters of the galaxies associated with high-metallicity DLAs at $z \approx 2$ are typically $\lesssim$30 kpc. We argue that high-metallicity galaxies are likely to have a large H I mass, and hence a large H I spatial extent. High-metallicity DLAs at $z \approx 2$ are thus likely to arise in the H I reservoirs of massive galaxies.

Finally, we found that galaxies associated with high-metallicity DLAs ($[M/H] > -0.3$) may remain unidentified in both CO searches (if they do not have extreme molecular gas masses) and Lyα searches (due to high dust obscuration). Searches in the Hα, [O III]λ5007, and [C II] 158 μm lines will likely be necessary to identify this population.

Acknowledgments

We thank the reviewer for detailed comments on an earlier version of this manuscript. This material is based upon work supported by the National Science Foundation under grants AST-2107989 and AST-2107990. M.R. also acknowledges support from the STScI's Director's Discretionary Research Funding (grant ID D0101.90306). R.A.J. gratefully acknowledges support from the Nantucket Maria Mitchell Association. N.K. acknowledges the Department of Atomic Energy for funding support, under project 12-R&D-TFR-5.02-0700. The data presented herein were obtained at the W. M. Keck Observatory, which is operated as a scientific partnership among the California Institute of Technology, the University of California, and the National Aeronautics and Space Administration. The Observatory was made possible by the generous financial support of the W. M. Keck Foundation. The authors wish to recognize and acknowledge the very significant cultural role and reverence that the summit of Maunakea has always had within the indigenous Hawaiian community. We are most fortunate to have the opportunity to conduct observations from this mountain.

ORCID iDs

Grecco A. Oyarzún https://orcid.org/0000-0003-0028-4130
Marc Rafelski https://orcid.org/0000-0002-9946-4731
Nissim Kanekar https://orcid.org/0000-0002-9757-7206
J. Xavier Prochaska https://orcid.org/0000-0002-7738-6875
Marcel Neeleman https://orcid.org/0000-0002-9838-8191
Regina A. Jorgenson https://orcid.org/0000-0003-2973-0472

References

Alam, S., Albareti, F. D., Allende Prieto, C., et al. 2015, ApJS, 219, 12
Arrigoni Battaia, F., Hennawi, J. F., Cantalupo, S., & Prochaska, J. X. 2016, ApJ, 829, 3
Arrigoni Battaia, F., Hennawi, J. F., Prochaska, J. X., et al. 2019, MNRAS, 482, 3162
Atek, H., Kunth, D., Schaerer, D., et al. 2014, A&A, 561, A89
Balashev, S. A., Noterdaeme, P., Rahmani, H., et al. 2017, MNRAS, 470, 2890
Begum, A., Chengalur, J. N., Karachentsev, I. D., Sharina, M. E., & Kaisin, S. S. 2008, MNRAS, 386, 1667
Bera, A., Kanekar, N., Chengalur, J. N., & Bagla, J. S. 2019, ApJL, 882, L7
Berg, T. A. M., Neeleman, M., Prochaska, J. X., Ellison, S. L., & Wolfe, A. M. 2015, PASP, 127, 167
Blanc, G. A., Adams, J. J., Gebhardt, K., et al. 2011, ApJ, 736, 31
Bolatto, A. D., Wolfire, M., & Leroy, A. K. 2013, ARA&A, 51, 207
Broeils, A. H., & Rhee, M. H. 1997, A&A, 324, 877
Cai, Z., Cantalupo, S., Prochaska, J. X., et al. 2019, ApJS, 245, 23
Cassata, P., Tasca, L. A. M., Le Fèvre, O., et al. 2015, A&A, 573, A24
Catinella, B., Saintonge, A., Janowiecki, S., et al. 2018, MNRAS, 476, 875
Chabrier, G. 2003, PASP, 115, 763

Charlot, S., & Fall, S. M. 1993, ApJ, 415, 580
Chowdhury, A., Kanekar, N., & Chengalur, J. N. 2022a, ApJ, 937, 103
Chowdhury, A., Kanekar, N., & Chengalur, J. N. 2022b, ApJL, 935, L5
Chowdhury, A., Kanekar, N., Chengalur, J. N., Sethi, S., & Dwarakanath, K. S. 2020, Natur, 586, 369
Chowdhury, A., Kanekar, N., Das, B., Dwarakanath, K. S., & Sethi, S. 2021, ApJL, 913, L24
Christensen, L., Møller, P., Fynbo, J. P. U., & Zafar, T. 2014, MNRAS, 445, 225
Christensen, L., Wisotzki, L., Roth, M. M., et al. 2007, A&A, 468, 587
Chung, A., van Gorkom, J. H., Kenney, J. D. P., Crowl, H., & Vollmer, B. 2009, AJ, 138, 1741
Ciardullo, R., Zeimann, G. R., Gronwall, C., et al. 2014, ApJ, 796, 64
Cortese, L., Catinella, B., & Smith, R. 2021, PASA, 38, e035
Crighton, N. H. M., Murphy, M. T., Prochaska, J. X., et al. 2015, MNRAS, 452, 217
Dijkstra, M., & Kramer, R. 2012, MNRAS, 424, 1672
Duval, F., Schaerer, D., Östlin, G., & Laursen, P. 2014, A&A, 562, A52
Erb, D. K., Shapley, A. E., Pettini, M., et al. 2006, ApJ, 644, 813
Farina, E. P., Arrigoni-Battaia, F., Costa, T., et al. 2019, ApJ, 887, 196
Farina, E. P., Venemans, B. P., Decarli, R., et al. 2017, ApJ, 848, 78
Fernández, X., Gim, H. B., van Gorkom, J. H., et al. 2016, ApJL, 824, L1
Finlator, K., Davé, R., & Oppenheimer, B. D. 2007, MNRAS, 376, 1861
Fitzpatrick, E. L. 1999, PASP, 111, 63
Fumagalli, M., Mackenzie, R., Trayford, J., et al. 2017, MNRAS, 471, 3686
Fumagalli, M., O'Meara, J. M., Prochaska, J. X., Rafelski, M., & Kanekar, N. 2015, MNRAS, 446, 3178
Fynbo, J. P. U., Christensen, L., Geier, S. J., et al. 2023, A&A, 679, A30
Fynbo, J. P. U., Geier, S. J., Christensen, L., et al. 2013, MNRAS, 436, 361
Fynbo, J. P. U., Heintz, K. E., Neeleman, M., et al. 2018, MNRAS, 479, 2126
Fynbo, J. P. U., Laursen, P., Ledoux, C., et al. 2010, MNRAS, 408, 2128
Fynbo, J. P. U., Ledoux, C., Møller, P., Thomsen, B., & Burud, I. 2003, A&A, 407, 147
Fynbo, J. P. U., Ledoux, C., Noterdaeme, P., et al. 2011, MNRAS, 413, 2481
Fynbo, J. P. U., Prochaska, J. X., Sommer-Larsen, J., Dessauges-Zavadsky, M., & Møller, P. 2008, ApJ, 683, 321
Gaia Collaboration, Vallenari, A., Brown, A. G. A., et al. 2023, A&A, 674, A1
Gallazzi, A. R., Pasquali, A., Zibetti, S., & La Barbera, F. 2021, MNRAS, 502, 4457
Giavalisco, M., Macchetto, F. D., & Sparks, W. B. 1994, A&A, 288, 103
Gronke, M., & Dijkstra, M. 2016, ApJ, 826, 14
Gronke, M., Dijkstra, M., McCourt, M., & Oh, S. P. 2016, ApJL, 833, L26
Gronwall, C., Ciardullo, R., Hickey, T., et al. 2007, ApJ, 667, 79
Grove, L. F., Fynbo, J. P. U., Ledoux, C., et al. 2009, A&A, 497, 689
Guaita, L., Gawiser, E., Padilla, N., et al. 2010, ApJ, 714, 255
Gunn, J. E., & Gott, J. R. I. 1972, ApJ, 176, 1
Hayes, M., Schaerer, D., Östlin, G., et al. 2011, ApJ, 730, 8
Haynes, M. P., Giovanelli, R., Kent, B. R., et al. 2018, ApJ, 861, 49
Heald, G., Józsa, G., Serra, P., et al. 2011, A&A, 526, A118
Herenz, E. C., Wisotzki, L., Roth, M., & Anders, F. 2015, A&A, 576, A115
Jiang, L., Egami, E., Mechtley, M., et al. 2013, ApJ, 772, 99
Jones, M. G., Haynes, M. P., Giovanelli, R., & Moorman, C. 2018, MNRAS, 477, 2
Jorgenson, R. A., Murphy, M. T., & Thompson, R. 2013, MNRAS, 435, 482
Jorgenson, R. A., & Wolfe, A. M. 2014, ApJ, 785, 16
Joshi, R., Fumagalli, M., Srianand, R., et al. 2021, ApJ, 908, 129
Kanekar, N., Prochaska, J. X., Neeleman, M., et al. 2020, ApJL, 901, L5
Kanekar, N., Prochaska, J. X., Smette, A., et al. 2014, MNRAS, 438, 2131
Kaplan, K. F., Prochaska, J. X., Herbert-Fort, S., Ellison, S. L., & Dessauges-Zavadsky, M. 2010, PASP, 122, 619
Kaur, B., Kanekar, N., Rafelski, M., et al. 2021, ApJ, 921, 68
Kaur, B., Kanekar, N., Rafelski, M., et al. 2022a, ApJL, 933, L42
Kaur, B., Kanekar, N., Revalski, M., et al. 2022b, ApJ, 934, 87
Kawata, D., & Mulchaey, J. S. 2008, ApJL, 672, L103
Kennicutt, R. C., & Evans, N. J. 2012, ARA&A, 50, 531
Kereš, D., Katz, N., Weinberg, D. H., & Davé, R. 2005, MNRAS, 363, 2
Klimenko, V. V., Petitjean, P., & Ivanchik, A. V. 2020, MNRAS, 493, 5743
Krogager, J.-K., Fynbo, J. P. U., Ledoux, C., et al. 2013, MNRAS, 433, 3091
Krogager, J. K., Fynbo, J. P. U., Noterdaeme, P., et al. 2016, MNRAS, 455, 2698
Krogager, J. K., Møller, P., Fynbo, J. P. U., & Noterdaeme, P. 2017, MNRAS, 469, 2959
Kulkarni, V. P., Woodgate, B. E., York, D. G., et al. 2006, ApJ, 636, 30
Laursen, P., Sommer-Larsen, J., & Andersen, A. C. 2009, ApJ, 704, 1640
Ledoux, C., Petitjean, P., Fynbo, J. P. U., Møller, P., & Srianand, R. 2006, A&A, 457, 71
Leroy, A. K., Walter, F., Brinks, E., et al. 2008, AJ, 136, 2782
Lofthouse, E. K., Fumagalli, M., Fossati, M., et al. 2020, MNRAS, 491, 2057
Lofthouse, E. K., Fumagalli, M., Fossati, M., et al. 2023, MNRAS, 518, 305
Lowenthal, J. D., Hogan, C. J., Green, R. F., et al. 1991, ApJL, 377, L73
Mackenzie, R., Fumagalli, M., Theuns, T., et al. 2019, MNRAS, 487, 5070
Matthee, J., Sobral, D., Oteo, I., et al. 2016, MNRAS, 458, 449
Mawatari, K., Yamada, T., Nakamura, Y., Hayashino, T., & Matsuda, Y. 2012, ApJ, 759, 133
Mérida, R. M., Pérez-González, P. G., Sánchez-Blázquez, P., et al. 2023, ApJ, 950, 125
Møller, P., Fynbo, J. P. U., & Fall, S. M. 2004, A&A, 422, L33
Møller, P., Fynbo, J. P. U., Ledoux, C., & Nilsson, K. K. 2013, MNRAS, 430, 2680
Møller, P., & Warren, S. J. 1993, A&A, 270, 43
Møller, P., Warren, S. J., Fall, S. M., Fynbo, J. U., & Jakobsen, P. 2002, ApJ, 574, 51
Morrissey, P., Matuszewski, M., Martin, D. C., et al. 2018, ApJ, 864, 93
Neeleman, M., Kanekar, N., Prochaska, J. X., et al. 2017, Sci, 355, 1285
Neeleman, M., Kanekar, N., Prochaska, J. X., et al. 2018, ApJL, 856, L12
Neeleman, M., Kanekar, N., Prochaska, J. X., Rafelski, M. A., & Carilli, C. L. 2019, ApJL, 870, L19
Neeleman, M., Prochaska, J. X., & Wolfe, A. M. 2015, ApJ, 800, 7
Neeleman, M., Wolfe, A. M., Prochaska, J. X., & Rafelski, M. 2013, ApJ, 769, 54
Nielsen, N. M., Kacprzak, G. G., Sameer, et al. 2022, MNRAS, 514, 6074
Nilsson, K. K., Möller-Nilsson, O., Møller, P., Fynbo, J. P. U., & Shapley, A. E. 2009, MNRAS, 400, 232
Noterdaeme, P., Ledoux, C., Petitjean, P., & Srianand, R. 2008, A&A, 481, 327
Noterdaeme, P., Petitjean, P., Carithers, W. C., et al. 2012, A&A, 547, L1
Oke, J. B., & Gunn, J. E. 1983, ApJ, 266, 713
O'Sullivan, D. B., Martin, C., Matuszewski, M., et al. 2020, ApJ, 894, 3
Oyarzún, G. A., Blanc, G. A., González, V., et al. 2016, ApJL, 821, L14
Oyarzún, G. A., Blanc, G. A., González, V., Mateo, M., & Bailey, J. I. I. 2017, ApJ, 843, 133
Oyarzún, G. A., Bundy, K., Westfall, K. B., et al. 2023, ApJ, 947, 13
Pasquali, A., Gallazzi, A., Fontanot, F., et al. 2010, MNRAS, 407, 937
Péroux, C., Bouché, N., Kulkarni, V. P., York, D. G., & Vladilo, G. 2011, MNRAS, 410, 2237
Péroux, C., Bouché, N., Kulkarni, V. P., York, D. G., & Vladilo, G. 2012, MNRAS, 419, 3060
Prochaska, J. X., Hennawi, J. F., Lee, K.-G., et al. 2013, ApJ, 776, 136
Prochaska, J. X., Herbert-Fort, S., & Wolfe, A. M. 2005, ApJ, 635, 123
Prochaska, J. X., Neeleman, M., Kanekar, N., & Rafelski, M. 2019, ApJL, 886, L35
Prochaska, J. X., & Wolfe, A. M. 1997, ApJ, 487, 73
Rafelski, M., Neeleman, M., Fumagalli, M., Wolfe, A. M., & Prochaska, J. X. 2014, ApJL, 782, L29
Rafelski, M., Wolfe, A. M., Prochaska, J. X., Neeleman, M., & Mendez, A. J. 2012, ApJ, 755, 89
Rahmati, A., & Schaye, J. 2014, MNRAS, 438, 529
Rao, S. M., Turnshek, D. A., Sardane, G. M., & Monier, E. M. 2017, MNRAS, 471, 3428
Reddy, N. A., Steidel, C. C., Fadda, D., et al. 2006, ApJ, 644, 792
Rhodin, N. H. P., Agertz, O., Christensen, L., Renaud, F., & Fynbo, J. P. U. 2019, MNRAS, 488, 3634
Rivera-Thorsen, T. E., Hayes, M., Östlin, G., et al. 2015, ApJ, 805, 14
Roche, N., Humphrey, A., & Binette, L. 2014, MNRAS, 443, 3795
Schlafly, E. F., & Finkbeiner, D. P. 2011, ApJ, 737, 103
Schlegel, D. J., Finkbeiner, D. P., & Davis, M. 1998, ApJ, 500, 525
Shapley, A. E., Steidel, C. C., Pettini, M., & Adelberger, K. L. 2003, ApJ, 588, 65
Sheinis, A. I., Bolte, M., Epps, H. W., et al. 2002, PASP, 114, 851
Skelton, R. E., Whitaker, K. E., Momcheva, I. G., et al. 2014, ApJS, 214, 24
Smith, H. E., Cohen, R. D., Burns, J. E., Moore, D. J., & Uchida, B. A. 1989, ApJ, 347, 87
Sobral, D., & Matthee, J. 2019, A&A, 623, A157
Stark, D. P., Ellis, R. S., Bunker, A., et al. 2009, ApJ, 697, 1493
Steidel, C. C., Adelberger, K. L., Giavalisco, M., Dickinson, M., & Pettini, M. 1999, ApJ, 519, 1
Steidel, C. C., Adelberger, K. L., Shapley, A. E., et al. 2003, ApJ, 592, 728
Steidel, C. C., Giavalisco, M., Pettini, M., Dickinson, M., & Adelberger, K. L. 1996, ApJL, 462, L17
Stern, J., Sternberg, A., Faucher-Giguère, C.-A., et al. 2021, MNRAS, 507, 2869
Tacconi, L. J., Genzel, R., & Sternberg, A. 2020, ARA&A, 58, 157

Tremonti, C. A., Heckman, T. M., Kauffmann, G., et al. 2004, ApJ, 613, 898
Treu, T., Trenti, M., Stiavelli, M., Auger, M. W., & Bradley, L. D. 2012, ApJ, 747, 27
Trussler, J., Maiolino, R., Maraston, C., et al. 2021, MNRAS, 500, 4469
Tumlinson, J., Peeples, M. S., & Werk, J. K. 2017, ARA&A, 55, 389
Verhamme, A., Schaerer, D., Atek, H., & Tapken, C. 2008, A&A, 491, 89
Verhamme, A., Schaerer, D., & Maselli, A. 2006, A&A, 460, 397
Verheijen, M. A. W. 2001, ApJ, 563, 694
Vogt, S. S., Allen, S. L., Bigelow, B. C., et al. 1994, Proc. SPIE, 2198, 362
Walter, F., Brinks, E., de Blok, W. J. G., et al. 2008, AJ, 136, 2563
Walter, F., Carilli, C., Neeleman, M., et al. 2020, ApJ, 902, 111
Wang, J., Koribalski, B. S., Serra, P., et al. 2016, MNRAS, 460, 2143
Wang, W.-H., Kanekar, N., & Prochaska, J. X. 2015, MNRAS, 448, 2832
Werle, A., Poggianti, B., Moretti, A., et al. 2022, ApJ, 930, 43
Wetzel, A. R., Tinker, J. L., Conroy, C., & van den Bosch, F. C. 2013, MNRAS, 432, 336
Whitaker, K. E., Franx, M., Leja, J., et al. 2014, ApJ, 795, 104
Wolfe, A. M., Gawiser, E., & Prochaska, J. X. 2005, ARA&A, 43, 861
Zwaan, M. A., Meyer, M. J., Staveley-Smith, L., & Webster, R. L. 2005, MNRAS, 359, L30